eLife

Reviewed Preprint
v1 • July 3, 2026
Not revised

For correspondence:
paynea@janelia.hhmi.org

Competing interests: No competing interests declared

Funding: See page 30

Reviewing editor: Adrien Peyrache, McGill University, Canada

NPAS4 refines spatial and temporal firing in CA1 pyramidal neurons

Anja Payne[1,2], Daniel A Heinz[3], Chiaki Santiago[1,4], Lara L Hagopian[5,6], Rolando Sceptre Ganasi[5,7], Clare Quirk[3,8], Andrea L Hartzell[1,4], Jill K Leutgeb[5,9], Stefan Leutgeb[5,9], Brenda L Bloodgood[5]

[1]Neurosciences Graduate Program, UC San Diego, La Jolla, United States • [2]Janelia Research Campus, Howard Hughes Medical Institute, Ashburn, United States • [3]Biological Sciences PhD Program, UC San Diego, La Jolla, United States • [4]Neurocrine Biosciences, San Diego, United States • [5]Department of Neurobiology, School of Biological Sciences, UC San Diego, La Jolla, United States • [6]Neurosciences Graduate Program, UC San Francisco, San Francisco, United States • [7]UC Irvine School of Medicine, Irvine, United States • [8]Ionis Pharmaceuticals, Carlsbad, United States • [9]Kavli Institute for Brain and Mind, UC San Diego, La Jolla, United States

eLife Assessment

This **important** study shows that NPAS4, a gene that is switched on by neural activity, enhances the spatial and temporal precision of hippocampal neurons during navigation. These findings, based on selective and sparse gene deletion, are supported by **convincing** evidence. However, the experiments were performed entirely in animals exposed to long-term environmental enrichment, which leaves open the question of whether the same effects would emerge under standard housing conditions. This study will be of interest to neuroscientists studying neuronal circuits and spatial coding.

https://doi.org/10.7554/eLife.111430.1.sa3

Abstract

NPAS4 is an activity-dependent transcription factor that, in CA1 of the hippocampus, regulates inhibitory synapses made onto the active pyramidal neuron. In principle, NPAS4 thereby allows the past activity of a neuron to influence how it encodes information, although this has not yet been demonstrated. Here, we generated a sparse, CA1-specific knockout (KO) of NPAS4 in the mouse hippocampus and used optogenetic tagging to identify KO neurons *in vivo*. Recordings from intermingled wild-type (WT) and KO neurons in awake behaving animals revealed that NPAS4 deletion degrades spatial representations and temporal precision of spiking: KO neurons exhibited larger place fields with reduced in-field firing and increased out-of-field firing, less stable place fields, reduced coupling to local field potential theta oscillations, and diminished phase precession. These findings demonstrate that NPAS4 plays a crucial role in refining the spatial and temporal properties of CA1 pyramidal neuron spikes, which themselves are thought to be fundamental building blocks of more complex processes such as learning and memory.

Introduction

Experiences drive long-lasting changes in brain function through a range of molecular mechanisms, including the induction of activity-dependent transcription factors. These transcription factors are rapidly induced by transient neuronal activity and initiate gene expression programs that result in persistent alterations to neuronal function and synaptic connectivity[1–6]. Although a growing body of research has linked the expression of activity-dependent transcription factors to learning, memory, and behavior[7–12], relatively few studies have directly examined how these factors influence the encoding of information in awake, behaving animals[13–17].

In mice, the transcription factor NPAS4 is expressed almost exclusively in neurons and can be induced across multiple brain regions in a stimulus-dependent manner[13,18–25]. For instance, contextual fear conditioning or exposure to an enriched environment can elicit NPAS4 expression in behaviorally-relevant neuronal populations throughout the hippocampus[6,13,22–25]. In CA1 pyramidal neurons, NPAS4 deletion highlights its central role in modulating inhibitory input: knockout neurons exhibit reduced somatic and increased dendritic inhibition compared to neighboring wild-type neurons[6]. Importantly, these changes arise from the selective regulation of synapses formed by anatomically distinct populations of cholecystokinin (CCK)-expressing interneurons[22,25,26], indicating that NPAS4 expression reshapes how CA1 pyramidal neurons are integrated into the CCK inhibitory microcircuit.

During active exploration, a subset of CA1 pyramidal neurons fire in spatially selective patterns and show temporally organized spiking activity that is aligned to the ongoing theta rhythm. Individual pyramidal neurons can code for an animal's location with spatially-tuned firing that occurs when the animal is in the neuron's place field[27–30]. Place field firing is temporally coordinated with theta oscillations, which is the main oscillatory pattern during running. At the entrance into a place field, neurons fire late in the theta cycle, and at the exit, they fire early in the cycle. This phase precession orders the spiking of overlapping place fields such that a series of place fields along a spatial trajectory is also found in a time-compressed form within a theta cycle[31–37]. Recently, CCK+ inhibitory neurons have been shown to influence both the spatial and temporal firing of CA1 pyramidal neurons. Specifically, chronic dysregulation of CCK+ inhibitory neuron connectivity or deletion of cannabinoid receptors (CB1Rs) from CCK+ inhibitory neurons results in larger place fields recorded from CA1 pyramidal neurons[38,39]. Acute optogenetic silencing of CCK+ inhibitory neurons also leads to broader place fields and reveals a role for CCK+ inhibitory neurons in constraining burst firing and theta-phase precession of pyramidal neuron spiking[40]. Thus, the activity of CCK+ inhibitory neurons influences both the spatial and temporal tuning of pyramidal neurons, prompting us to hypothesize that NPAS4, as a transcriptional regulator of CCK+ inhibitory synapses, similarly refines pyramidal neuron firing.

To examine how NPAS4 influences spatial representations and temporal precision of spiking, we recorded CA1 pyramidal neuron firing in mice actively navigating a rectangular track, a behavioral context in which place fields and theta-phase–related firing patterns reliably emerge. We used viral expression of Cre to knockout *Npas4* and permit expression of Channelrhodopsin in the transduced CA1 pyramidal neurons. This enabled us to obtain extracellular optetrode recordings from intermingled wildtype (WT) and optotagged[41] NPAS4 knockout (KO) neurons during navigation. Importantly, sparse deletion of NPAS4 allows for direct comparisons between neurons of different "genotypes" within an individual animal and reduces non-cell autonomous network dysregulation, such as seizure activity[5], that occurs when NPAS4 is deleted from large populations of neurons. We observed that while NPAS4 KO neurons exhibited place fields, these fields were larger and less stable throughout the recording session in comparison to those recorded from WT neurons. In addition to these deficits in spatial representations, KO neuron firing was weakly coupled to theta oscillations and demonstrated less theta-phase precession. Collectively, these findings show that cell-specific loss of NPAS4 disrupts the spatial and temporal organization of CA1 pyramidal neuron activity, linking a transcriptional regulator of CCK+ inhibitory neurons to fundamental building blocks of higher-level cognition.

Results

NPAS4 Reorganizes Somatodendritic Inhibition in CA1 Pyramidal Neurons of Adult Mice

We confirmed that in CA1 of adult mice, NPAS4 is expressed in select neurons following exposure to an enriched environment (EE; Figure 1A). We next asked whether NPAS4 has the same effect on inhibitory circuit organization in adult mice as has been previously shown in juveniles[6,22,26]. To test this, we injected AAV.CamKII_Cre-GFP into the CA1 region of adult *Npas4*$^{fl/fl}$ mice (~postnatal day 70, P70). After recovery from the surgery, mice were housed in EE for 2-3 months

with regular updating of the environment to maintain novelty, matching the timeline used for separate experiments in which we obtained *in vivo* extracellular recordings. After the prolonged housing in EE, we prepared acute hippocampal slices and performed simultaneous whole-cell recordings from neighboring wild-type (WT) and NPAS4 knockout (KO) neurons. Electrical stimulation was delivered in the somatic or dendritic layers, and pharmacologically-isolated evoked inhibitory postsynaptic currents (eIPSCs) were recorded (Figures 1B and C). KO neurons had smaller amplitude somatic eIPSCs and larger amplitude dendritic eIPSCs than neighboring WT neurons (Figure 1C). Thus, NPAS4 shapes the distribution of inhibitory synaptic input onto CA1 pyramidal neurons in adulthood as it does in juveniles, and this synaptic phenotype persists with chronic exposure to EE.

Optical Tagging Enables *In Vivo* Identification of NPAS4 Knockout Neurons

We sought to determine how the loss of NPAS4 affects pyramidal neuronal firing in the context of an intact network with ongoing, behaviorally-driven network activity. To accomplish this, *Npas4*$^{fl/fl}$mice were crossed to Cre-dependent Channelrhodopsin-2 (ChR2) mice (*Npas4*$^{fl/fl}$:Ai32). Double-homozygous offspring were transduced with AAV.CamKII_Cre-GFP, resulting in an intermingled population of WT and KO neurons, where the KO neurons also expressed ChR2 (transduced neurons: 30-60%; Figure 1D, E, and S1). After recovery from surgery, mice were housed in EE for 2-3 months, including while electrophysiological recordings were obtained. Daily extracellular recordings were acquired first in the home cage, then during exploration of the rectangular track, and again in the home cage, with light stimulation delivered at the end of the final home cage session (Figure 1F). Spikes were sorted and clearly separated into clusters defined as a "unit", likely corresponding to spikes generated by a single neuron. In addition, units were well-isolated in both the pre-track and post-track home cage recording periods, demonstrating physical stability of the tetrode across the recording session (N = 174 units from 8 male mice, Figure S2E).

During opto-recording periods (10-30 minutes) at the end of each session, light was delivered through the optical fiber of the optetrode (pulsed at 0.5 Hz; pulse duration of 10 msec) with the laser power set to evoke a small light-triggered response in the LFP without evoking a population spike (typically ~3 mW; Figures S2A and S2C). Peristimulus time histograms (PSTH) were generated for each unit and the opto-response was calculated as the difference between the maximum spike count during the light pulse and the maximum spike count outside the pulse. Units that produced a reliable response to light stimulation were classified as NPAS4 KO neurons (opto-response > 1; n = 47 units), and units that did not were classified as "WT neurons" (opto-response < 1; n = 112 units; Figure 1G-H). Ambiguous units were excluded from further analysis (n = 15 units). KO neurons that express low levels of ChR2 might not robustly respond to the low-power light delivered, leading to some KO neurons being misclassified as WTs. To confirm the veracity of our WT population, we delivered high-power light, causing opto-triggered spikes from KO neurons to be recruited into the population spike and leaving WT neurons unchanged (Figures 1I, S2B, and S2D). Clusters of spikes from WT or KO neurons had comparable separation metrics and were present throughout the recording session (Figure S2E-H). Finally, percentages of KO neurons mirrored *post hoc* quantification of transduction density across animals (Figures S2I and S2J). Collectively, these analyses gave us confidence in our assignment of WT or KO neurons from tetrode recordings.

Spatial Tuning Is Impaired in NPAS4 Knockout CA1 Neurons

Given the role of CCK+ interneurons in sculpting spatial tuning, we hypothesized that the dysregulation of inhibitory input onto NPAS4 KO neurons would lead to aberrant activity patterns during navigation. To explore this, we compared WT and KO neuron firing while mice ran laps on the track for a food reward. Each track recording session consisted of 10 trials run in one direction (an epoch) followed by 10 trials run in the opposite direction, alternating for 8 epochs or 30 minutes, whichever came first (Figure 2A). Trained behavior across the track was stereotyped,

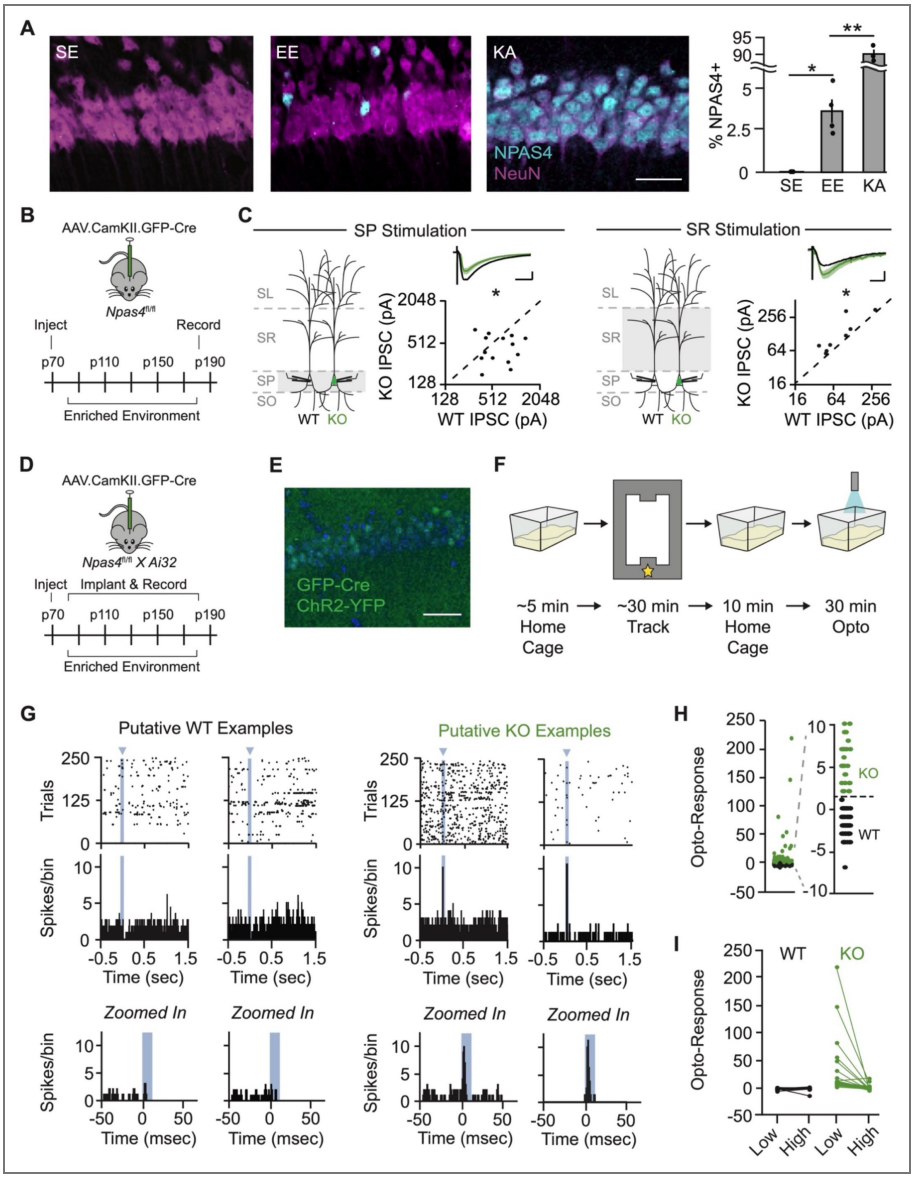

Figure 1. NPAS4 expression in CA1 pyramidal neurons in adult mice results in reorganization of inhibition along the somatodendritic axis.

(A) NPAS4 expression in CA1 from mice housed in a standard environment (SE), an enriched environment (EE) for 90 minutes, or following kainic acid (KA) injection. Magenta: NeuN; teal: NPAS4. Scale bar = 50 μm. (Data are mean ± SEM; SE: N = 3 animals, 3 sections each; EE: N = 4 animals, 3 sections each; KA: N = 3 animals, 3 sections each; unpaired t test.) (B) Schematic of the experimental strategy and timeline for whole-cell patch-clamp recordings. (C) eIPSCs evoked in either stratum pyramidale (SP) or stratum radiatum (SR) recorded with simultaneous voltage-clamp from neighboring WT (black) and KO (green) pyramidal neurons. Geometric mean traces shown as percent of WT. SP scale bar = 20 ms, 25% of WT; SR scale bar = 20 ms, 50% of WT. (SP: N = 14 slices from 6 mice; SR: N = 8 slices from 5 mice; ratio paired t test.) (D) Schematic of the experimental strategy and timeline for *in vivo* electrophysiology recordings. (E) Example image of sparse KO used for in vivo recordings. Scale bar = 50 μm. (F) Schematic of the experimental timeline for each session. Star: reward location. (G) Example rasters (top) and peristimulus time histograms (PSTH; middle) from putative WT (left) and KO (right) neurons. (Bottom) Same PSTHs as above, shown at higher temporal resolution to highlight the 1-second window surrounding light stimulation. Blue arrow and bars: light stimulation (WT example 1: Animal 6 WT Cell 2; WT example 2: Animal 2 WT Cell 3; KO example 1: Animal 1 KO Cell 1; KO example 2: Animal 5 KO Cell 1). (H) Opto-response during low-power light stimulation (~0.3 mW) in cells categorized as WT (black) or KO (green). Opto-response is defined as the peak PSTH value during light-on minus the peak PSTH value during light-off periods of the optostim protocol. (I) Opto-response during high-power light stimulation (>0.3 mW) in cells categorized as WT (black) or KO (green). As KO neurons were recruited into the pop-spike during high-power light stimulation, their opto-responses decrease substantially. *p < 0.05; **p < 0.01.

as assessed by velocity (Figures 2B and S2K-M). Across all trials on the track and considering only periods of time when the animal was running (velocity > 2 cm/sec), KO neurons had slightly but significantly higher firing rates than WT neurons (Figure 2C) but fewer spikes that occurred in bursts (defined as ISIs < 10 msec; Figures 2D and 2E).

It was unclear whether the increased firing rate measured in KO neurons reflected a more robust response within a neuron's place field or spurious firing outside the neuron's spatial receptive field. To disambiguate this, we analyzed spatial firing rates by linearizing the track (reward zone at 0) and calculating the spike rate within 4 cm bins (for example, see Figures S3A and B) when the animal was running (velocity > 2 cm/sec). Place fields are direction-selective[42,43]; thus, trials run in opposite directions (clockwise (CW) or counterclockwise (CCW)) were analyzed independently and considered as distinct data points.

To focus our analyses on neurons that are active during behavior, we classified neurons as "high firing" if their mean spatial firing rate exceeded 0.1 Hz and their trial-averaged maximum spatial firing rate exceeded 1 Hz (Figure 2G); neurons below this cutoff were classified as "low firing" (Figure 2F). Histograms of mean and maximum spatial firing rates revealed a continuous distribution in both genotypes (Figure S3C and D), underscoring that this classification is not categorical but instead provides a pragmatic cutoff to exclude cells with minimal spatially organized spiking.

NPAS4 WT and KO neurons had dramatically different percentages of neurons with low and high spatial firing rates during behavior. Among the WTs, ~27% of neurons had low firing rates in both directions, and 11% had low firing rates in one direction. In comparison, KO neurons were significantly different, with low firing rates in 11% of neurons in both directions and 17% in one direction (Figure 2H). Moreover, among the low firing rate neurons, KO neurons had significantly higher mean and maximum spatial firing rates (Figure 2I). In contrast, and despite the larger percentage of KO neurons in the high firing rate subgroup, we did not measure differences in the mean or maximum spatial firing rates between genotypes (Figure 2J). These results suggest that a greater proportion of KO neurons are active during behavior, possibly reducing the sparsity of the overall ensemble representation of the environment. Moreover, among the high firing rate neurons, the similarity between WT and KO spatial firing rates when averaged across the entire track raises the question of whether WT and KO neurons have comparable place field representations.

We considered the high firing rate neurons as putative place cells[29] and defined a place field as the contiguous bins in which the firing rate was above 10% max firing and at least one bin was above 50% max (Figure 3A). Both WT and KO place cells had comparable numbers of place fields (typically only one; Figure 3B) that tiled the track and were directionally selective (Figure 3C) with low Pearson's correlation coefficients between CW and CCW directions (Figure S3E). Despite these similarities, KO neurons generated significantly larger place fields than WT neurons (50 ± 3.52 cm and 39 ± 1.86 cm, respectively; Figure 3D).

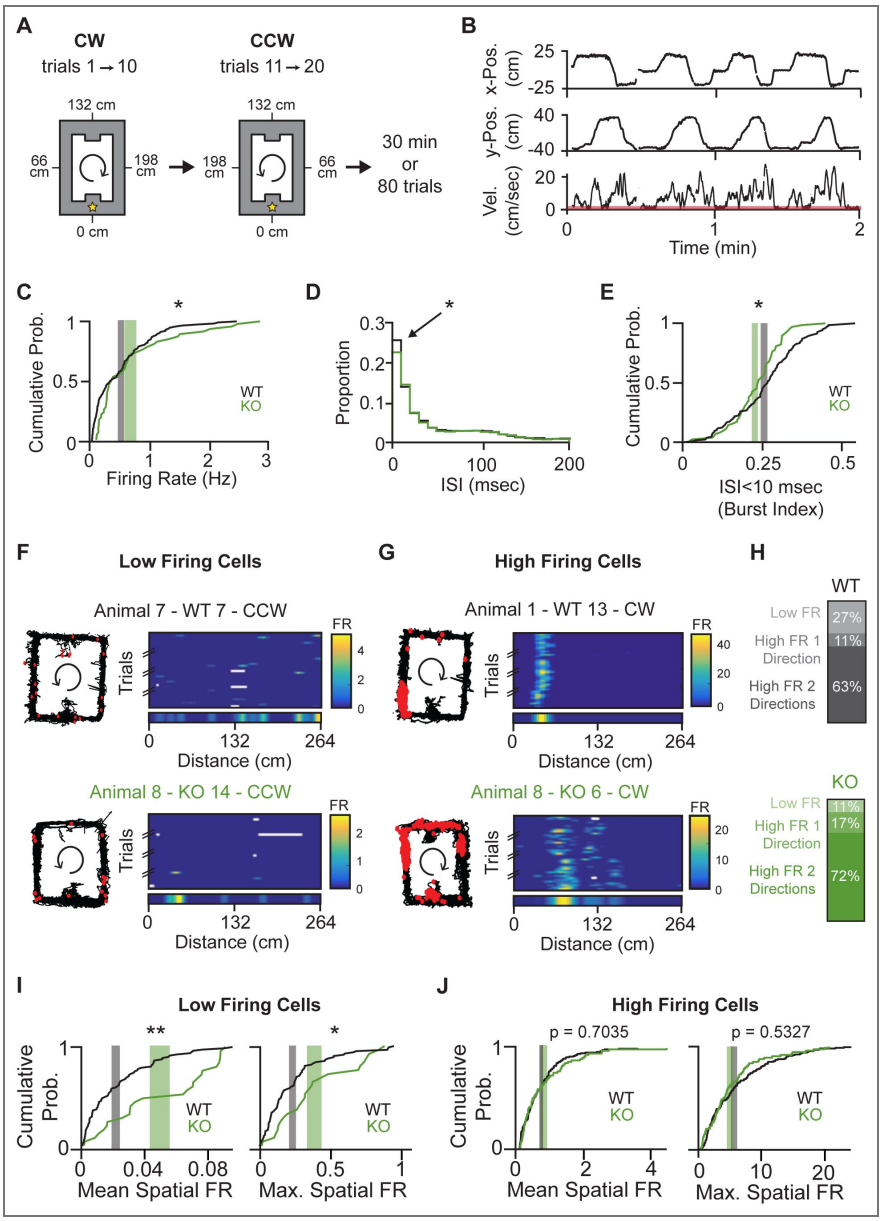

Figure 2. NPAS4 knockout neurons have fewer spikes in bursts and are more likely to have high firing rates, but high firing knockout and wild-type neurons exhibit comparable spatial firing.

(A) Schematic of the track recordings. Mice ran in one direction on a rectangular track for 10 trials before being required to switch directions. This behavior was repeated for up to 80 trials or 30 minutes, whichever occurred first. The track was linearized as indicated. (B) Example traces showing x-position (top), y-position (middle), and velocity (bottom) as an animal ran along the track. Time periods during which velocity fell below 2 cm/sec (red bar on velocity plot) were excluded from analysis. (C) Cumulative probability distribution of firing rates across the session. Firing rate was defined as the total number of spikes divided by session duration. Gray shaded region: ± SEM for WT, centered at the mean; green shaded region: ± SEM for KO, centered at the mean. (WT: N = 112 cells; KO: N = 47 cells; Kolmogorov–Smirnov test.) (D) Histogram of interspike intervals (ISIs). Arrow indicates ISIs < 10 ms. (WT: N = 112; KO: N = 47; Kolmogorov–Smirnov test.) (E) Cumulative probability distribution of the proportion of spikes in bursts, defined as ISIs < 10 ms. Shaded regions as in (C). (WT: N = 112; KO: N = 47; Kolmogorov–Smirnov test.) (F) Example linearized rate maps from a 'low firing' WT (top) and KO (bottom) neuron. Left: trajectory of the session (black), with spikes (red dots). Right: trial-by-trial linearized rate map for one direction, with the trial-averaged rate map shown below. (G) As in (F), but for 'high firing' WT and KO neurons. (H) Percentage of cells classified as 'low firing' or 'high firing' in one or both directions ($p < 0.05$; chi-square goodness-of-fit test) (I) Cumulative probability distributions of mean and maximum spatial firing rates for 'low firing' cells. Shaded regions as in (C) (WT: N = 86; KO: N = 26; Kolmogorov–Smirnov test). (J) As in (I), but for 'high firing' cells. (WT: N = 138; KO: N = 68; Kolmogorov–Smirnov test.) *$p < 0.05$; **$p < 0.01$.

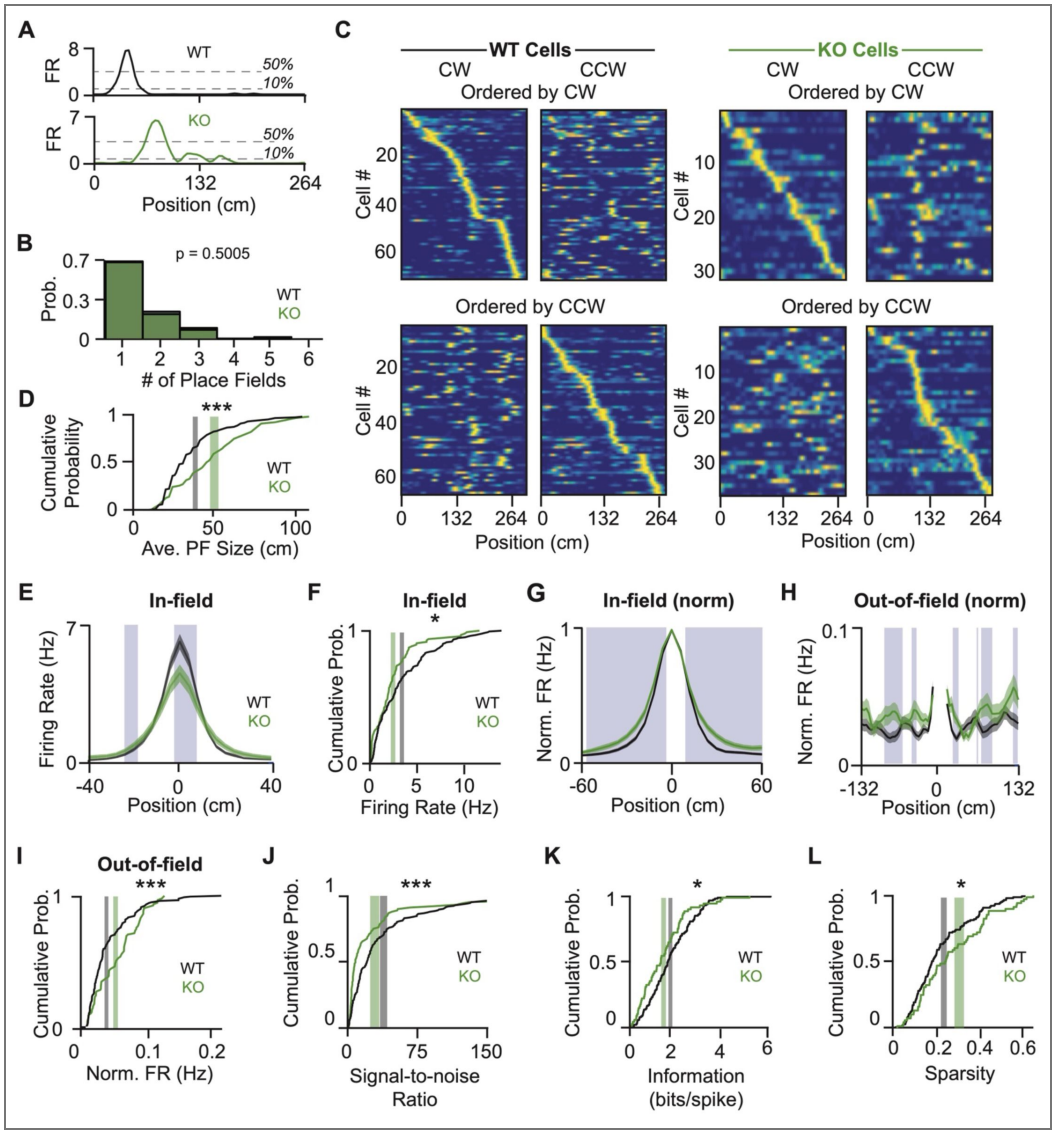

Figure 3. NPAS4 knockout neurons are less spatially tuned than simultaneously recorded wild-type counterparts.

(A) Example trial-averaged rate maps from a WT (top) and KO (bottom) neuron. Dotted lines mark 10% and 50% of the peak rate and were used to identify place fields (WT example: Animal 1, WT Cell 35; KO example: Animal 6, KO Cell 2). (B) Histogram of the number of place fields per neuron (WT: N = 138; KO: N = 68; Mann–Whitney test). (C) Trial-averaged rate maps from WT (left) and KO (right) neurons. Top: ordered by the peak location in the clockwise (CW) direction, with the same order applied to activity in the counterclockwise (CCW) direction. Bottom: ordered by peak location in the CCW direction (WT: N = 138; KO: N = 68). (D) Cumulative probability distribution of average place field size. Place fields were defined as sets of contiguous bins above 10% of the peak that also included at least one bin above 50%. Gray shaded region: ± SEM for WT, centered at the mean; green shaded region: ± SEM for KO, centered at the mean (WT: N = 138; KO: N = 68; Kolmogorov–Smirnov test). (E) Trial-averaged in-field rates for WT and KO place fields, centered on the peak of each field. Blue shaded regions indicate bins with $p < 0.05$ (WT: N = 183 fields over 138 neurons; KO: N = 95 fields over 68 neurons; Kolmogorov–Smirnov test). (F) Cumulative probability distribution of average in-field firing rates. Shaded regions as in (D) (WT: N = 138; KO: N = 68; Kolmogorov–Smirnov test). (G) As in (E), but firing rates normalized to each neuron's peak. (H) As in (G), but showing only out-of-field bins. (I) Cumulative probability distribution of average out-of-field firing rates. Shaded regions as in (D) (WT: N = 138; KO: N = 68; Kolmogorov–Smirnov test). (J) Cumulative probability distribution of signal-to-noise ratio, defined as the average in-field firing rate divided by the average out-of-field firing rate per neuron. Shaded regions as in (D) (WT: N = 138; KO: N = 68; Kolmogorov–Smirnov test). (K) Cumulative probability distribution of spatial information. Shaded regions as in (D) (WT: N = 138; KO: N = 68; Kolmogorov–Smirnov test). (L) Cumulative probability distribution of sparsity. Shaded regions as in (D) (WT: N = 138; KO: N = 68; Kolmogorov–Smirnov test). *$p < 0.05$; ***$p < 0.001$.

Our observation that WT and KO neurons have comparable spatial firing rates across the entire track, but KO neurons have larger place fields and thus larger portions of the track with elevated firing, presents a conundrum. One possible way to reconcile these measurements, particularly considering the excessive dendritic and reduced somatic inhibition received by NPAS4 KO neurons, would be if KO neurons have relatively lower firing rates within the place field and higher firing rates outside of the place field. Among WT neurons, 69% of action potentials were within the place field ("in-field") and 31% were distributed across the rest of the track ("out-of-field"); for KO neurons these values were 63% and 37%, respectively (Figure S3F). To quantify in-field spatial firing rates, we aligned each field to the peak and compared the firing rates in each spatial bin (Figure 3E). Across the population, KO neurons had significantly lower peak firing rates and reduced in-field firing rates (Figures 3E, 3F). After normalizing to the peak firing, KO neurons showed significantly higher firing rates as the animal entered and exited the field, driving the larger normalized place fields (Figure 3G). Moreover, increasing the firing rate threshold for defining a place field eliminated the differences between genotypes (Figures S3G and S3H), suggesting that place fields generated by KO neurons are not scaled versions of WT place fields.

If the overall spatial firing rates are comparable but the in-field firing rate is lower, KO neurons must have higher out-of-field firing. Indeed, in our normalized, peak-aligned rate maps, KO neurons often had higher out-of-field firing rates, and this was significant when averaging across all out-of-field bins (Figures 3H, 3I). The shift in spikes from in-field ("signal") to out-of-field ("noise") strongly reduced the KO neurons' signal-to-noise ratio (Figure 3J). Indeed, KO place cells conveyed less spatial information with each spike and fired more uniformly over the track (Figures 3K, 3L). These results were robust to variations in firing rate threshold (Figures S4A-C) and persisted when controlling for firing rate (Figures S4D-G). Thus, deleting NPAS4 reduces the precision of CA1 pyramidal neuron spatial representations.

Stability of Spatial Firing Is Reduced in NPAS4 Knockout Neurons

In the average rate maps, the KO neurons have significantly broader spatial tuning than WT neurons. Surprisingly, this difference seemed less prominent when looking at individual trials (Figures S5A–F). Place fields that shift location on a trial-to-trial basis could give the appearance of a larger average field while masking an underlying instability of the field. To assess place field stability, we averaged firing across the track for each epoch (10 trials) and calculated Pearson's correlation coefficients (PCCs) between successive epochs for WT and KO neurons. While both WT and KO neurons had PCCs that were higher than shuffles, the PCC was lower for KO neurons at each comparison, demonstrating that the overall spatial firing was less consistent across epochs (Figures 4A, 4B, and S5G). Restricting the analysis to in-field or out-of-field bins also revealed lower correlations in KO neuron firing (Figure S5H and S5I), suggesting that their place fields are more labile, and that the higher out-of-field activity measured in the KO neurons is spurious and unlikely to be nascent field formation.

Is the reduced correlation across epochs due to a systematic change in KO neuron spatial firing? To assess this, each place field was aligned to its peak location in the first epoch (E1; Figure 4C) and fields from all neurons were averaged within each epoch. In WT neurons, place fields remained stable across the first three epochs, but in E4, they showed a reduction in peak firing and a broader tail extending toward the field entrance—hinting at the Mehta effect[44,45] and behavioral timescale plasticity[46]. In contrast, KO neurons were indistinguishable from WTs in E1, but as early as E2, the average field began to degenerate, with reduced peak firing and increased activity in peri-field and out-of-field regions. These differences were exacerbated in the population averages in E3 and E4, indicating substantial heterogeneity in the changes exhibited by KO neurons.

To better understand how place fields changed at the level of individual neurons, we examined the shift in peak firing location across epochs. WT neurons showed minimal movement of the place field peak through E3, but by E4, over half of the fields had shifted toward the field entrance. KO neurons also showed shifts in peak firing towards the entrance, but these differences emerged as early as E2 (Figure S5J and S5K). To visualize changes in spatial firing across the entire track—

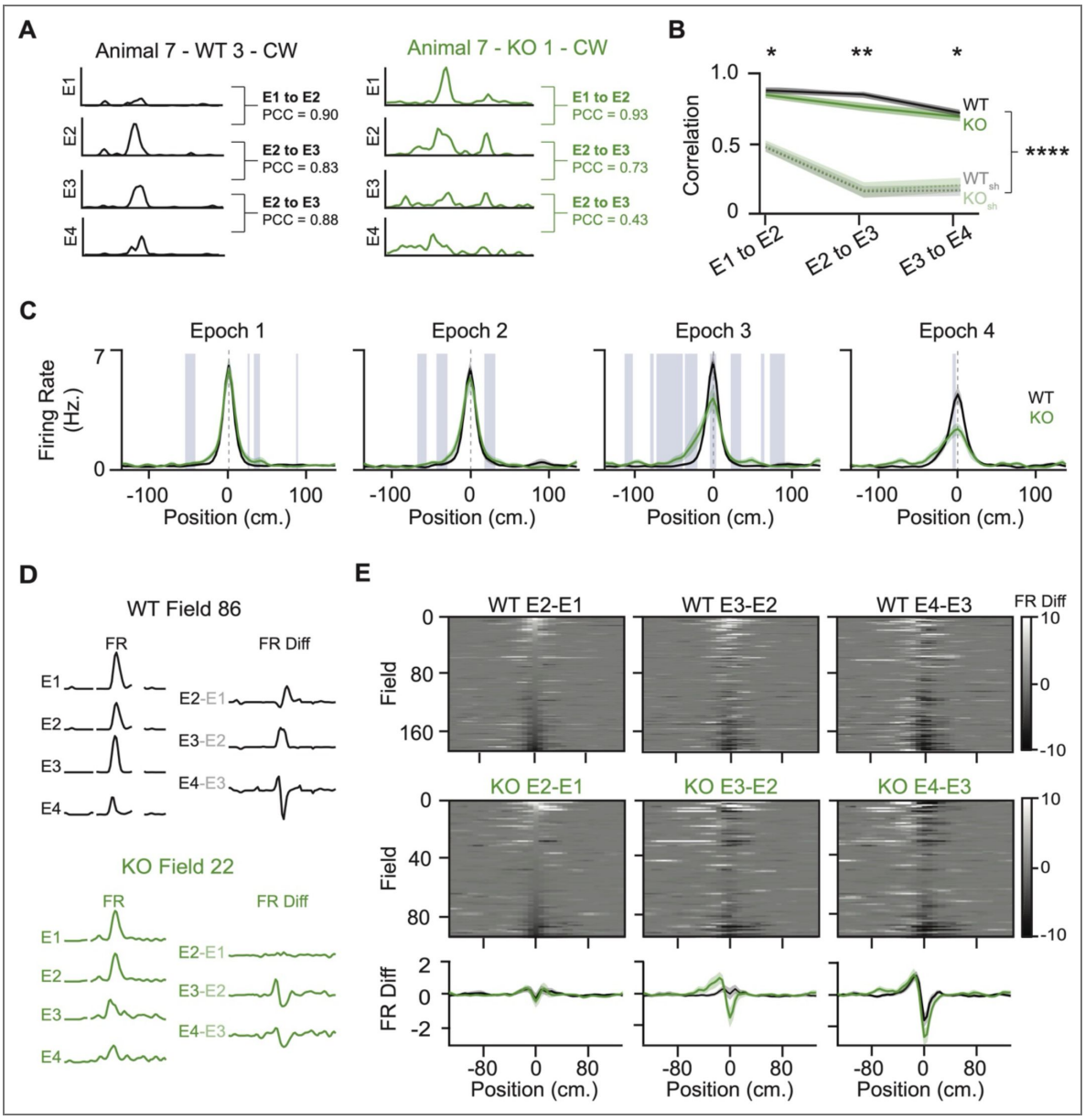

Figure 4. NPAS4 knockout neurons are less stable and shift their place fields towards the field entrance more rapidly than wild types.

(A) Example trial-averaged rate maps from each of the four epochs (sets of 10 trials) for a WT (left) and KO (right) neuron. For each pairwise comparison (epoch 1 to 2, epoch 2 to 3, and epoch 3 to 4), the Pearson's Correlation Coefficient (PCC) was calculated. (B) PCC across sequential epoch comparisons for WT (solid black) and KO (solid green) neurons, alongside shuffled controls (WT shuffle: dotted gray; KO shuffle: dotted green). Shuffled distributions were generated by spatially shifting trials randomly (WT: N = 138; KO: N = 68; Kolmogorov–Smirnov test for WT vs. KO; Wilcoxon signed-rank test for comparisons to shuffled distributions). (C) Trial-averaged rate maps for WT and KO place cells, separated by epoch and centered on the peak in Epoch 1. Blue shaded regions indicate bins where $p < 0.05$ (WT: N = 138; KO: N = 68; Kolmogorov–Smirnov test). (D) Example showing how difference maps are generated: trial-averaged rate maps from each epoch are centered on the peak of Epoch 1, and the difference between sequential epochs is computed. (E) Difference maps for WT (top) and KO (bottom) place fields across all epoch comparisons. Mean difference maps across neurons are shown below (WT: N = 176 fields from 138 neurons; KO: N = 91 fields from 68 neurons). *$p < 0.05$; **$p < 0.01$; ****$p < 0.0001$.

not just at the peak—for each neuron and across epochs, we computed firing rate difference maps between successive epochs. Each map was centered on the peak firing location from E1, and fields were ordered based on the change in firing between E2 and E1 across all comparisons (Figures 4D and 4E). Although there were a variety of responses within both populations, many place fields from WT neurons showed the characteristic Mehta effect at the level of individual cells, most consistently between E3 and E4[44,45]. KO neuron place field locations were more variable, with individual field positions jumping larger distances, often in early epochs, and without stability of the new location in subsequent epochs. Collectively, these analyses show that while place fields from both WT and KO neurons shift over time, the KO neuron place fields are exceptionally labile, likely underlying the larger trial-averaged field sizes and emerging from the dysregulation of inhibition.

Temporal Precision of Spiking Is Impaired in NPAS4 Knockout CA1 Neuron

During running, CA1 pyramidal neuron firing is organized with respect to the underlying theta rhythm in the local field potential (LFP). While phase precession broadens the range of theta phases at which CA1 pyramidal neurons fire, spiking remains largely confined to a preferred portion of the theta cycle[31–34]—[a] constraint shaped in part by rhythmic inhibition[40,47–50]. This led us to examine whether theta-phase coupling is disrupted in KO neurons.

In our experiments, KO and WT neurons are intermingled; hence, spikes generated by neurons of either genotype are aligned to a shared LFP. During bouts of running, the theta power in the LFP was indistinguishable from control-injected animals, indicating that sparse deletion of *Npas4* did not impact theta oscillations (Figure S6A and B). We filtered the LFP (2-20 Hz) to focus on the theta band and obtained the phase of theta at which each spike occurred, where 0° is the peak of theta and 180° is the trough (Figure 5A). We fit a vector to the spike-theta phases and used this to calculate the mean vector length (MVL) and the preferred theta phase for the best field (field with the highest firing rate) of each cell (Figure 5B). Although we did not observe any significant differences in the preferred theta phase between WT and KO populations (Figure 5C and D), we did find that KO cells had significantly lower MVLs (Figure 5E), indicating that the KO neurons have a weaker phase preference. This difference persisted when we considered in-field activity from all fields. No difference between WT and KO theta-phase coupling was detected when restricting the analysis to out-of-field firing (Figure S6C-E). The strength of theta coupling varies as an animal traverses a given neuron's place field, decreasing at the peak of the field[51,52]. We observed this pattern for both WT and KO firing. KO neurons, however, had considerably lower MVLs regardless of place field position (Figure 5F). Taken together, these data demonstrate that KO neuron place field firing is less theta-coupled than WT neuron counterparts.

Phase precession relies on spike timing across the theta cycle, wherein a pyramidal neuron's spikes occur at earlier phases of theta as the animal moves through its place field. This enables information about the sequential activation of fields to be preserved in the temporal ordering of spikes for fields with spatial overlap. Since KO neurons have reduced theta-phase coupling, we extended our analysis to phase precession to determine if there are also differences. For each trial, we plotted each spike's theta phase relative to the animal's location in the place field (Figure 6A) and used the slope of the linear fit to quantify phase precession (Figure 6B and C)[37,53,54]. For trials that met established criteria[55] (Figure S6F), trial-to-trial variability in slope did not differ between genotypes (Figure S6G). However, the mean slope per neuron (Figure 6D; median slopes: Figure S6N)—a measure of overall phase precession strength—was significantly shallower in KO neurons, despite both groups showing the expected negative values indicative of phase precession. This difference disappeared when we shuffled spike phases or spatial positions (Figure S6H-K) and remained robust to bootstrapping (Figures S6L and S6M). Thus, NPAS4 KO neurons have weaker phase precession than WT neurons.

Larger place fields have shallower phase precession[54,56], raising the possibility that field size differences could account for the diminished phase precession observed in KO neurons. First, considering the trials that met the criteria above and calculating field size for each trial

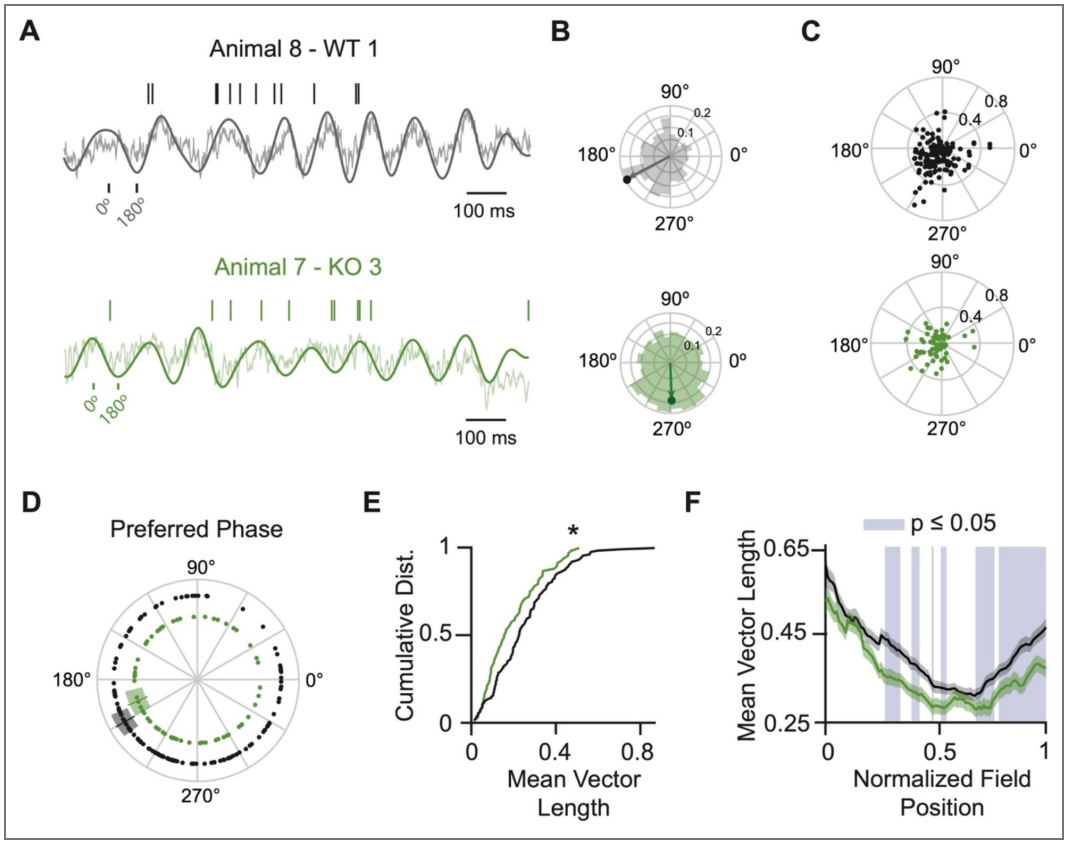

Figure 5. NPAS4 knockout cells are less theta-coupled than wild-type counterparts.

(A) Example of spiking relative to the local field potential (LFP) for WT (top) and KO (bottom) neurons. Spikes are shown as vertical lines above the raw LFP trace with the theta-filtered LFP overlaid. (B) Rose plots show the theta phase of all spikes from the same example neurons with the mean vector overlaid. (C) Rose plot scatter for all neurons. Angular position indicates preferred theta phase; radial position indicates mean vector length (WT: N = 138; KO: N = 68). (D) Preferred phase for WT and KO neurons. Solid line: mean; shaded region: SEM. Concentric circles shown for visualization only (WT: N = 138; KO: N = 68). (E) Cumulative probability distribution of mean vector lengths. Gray shaded region: ± SEM for WT, centered at the mean; green shaded region: ± SEM for KO, centered at the mean (WT: N = 138; KO: N = 68; Kolmogorov–Smirnov test). (F) Mean vector length as a function of normalized field position. Blue shaded regions indicate bins where $p < 0.05$ (WT: N = 183 fields from 138 neurons; KO: N = 95 fields from 68 neurons; Kolmogorov–Smirnov test). *$p < 0.05$.

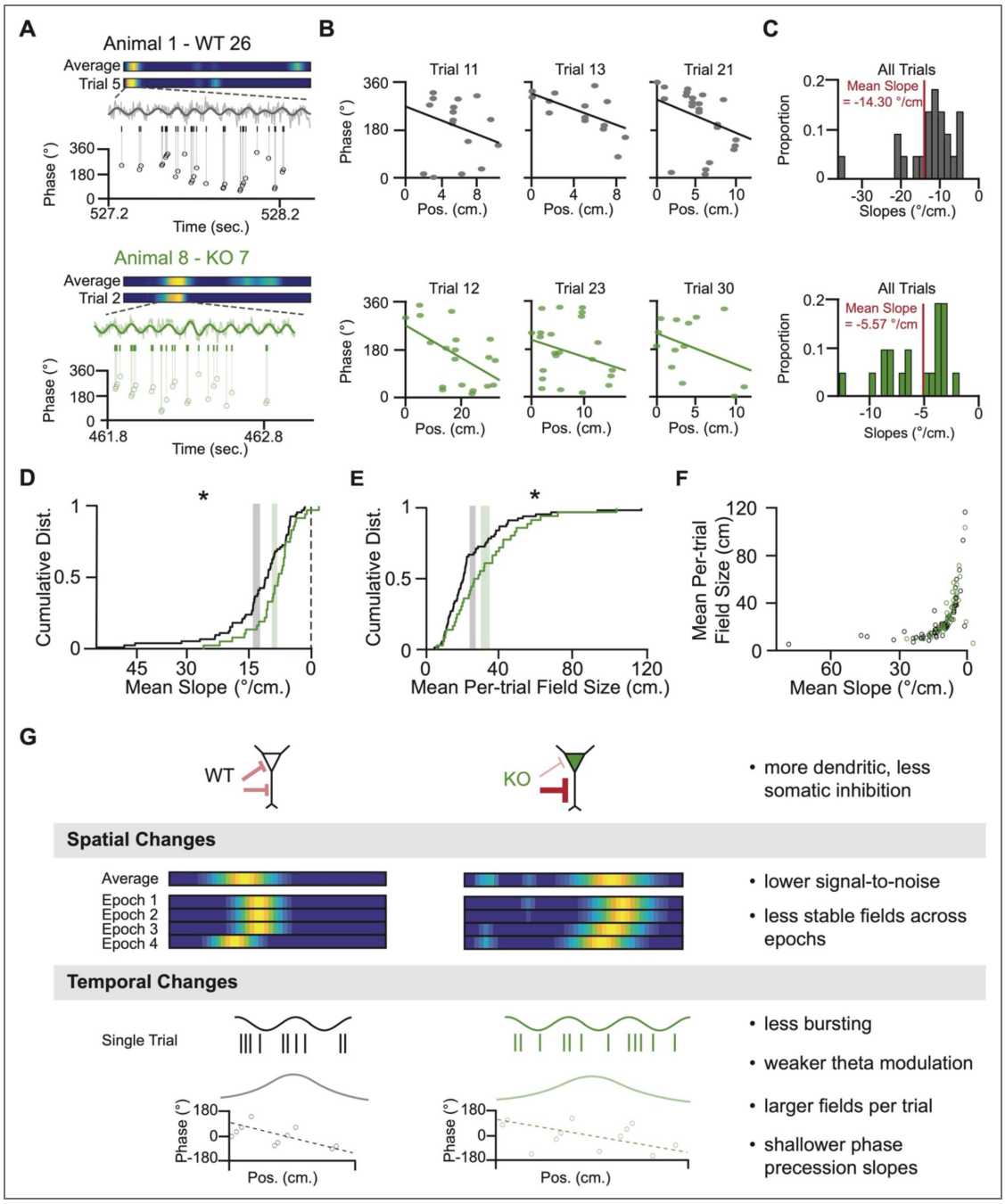

Figure 6. NPAS4 KO neurons exhibit shallower phase precession slopes compared to WT counterparts.

(A) Example WT (top) and KO (bottom) neurons showing theta-related spiking during a single field pass. For each example, the top panel shows the trial-averaged rate map across all trials; the panel immediately below shows the rate map for one example trial. The raw local field potential (LFP) during that trial is shown with the theta-filtered LFP overlaid. Spikes are marked as vertical lines below the LFP, and the theta phase of each spike is plotted over time. (B) Three example trials from the neurons shown in (A). Scatter plots show theta phase of each spike over position with linear fits overlaid. (C) Histogram of phase precession slopes across all trials for the neurons in (A). Red line: median slope. (D) Cumulative probability distribution of mean phase precession slopes. Only the field with the highest firing rate from each neuron is included. Gray shaded region: ± SEM for WT, centered at the mean; green shaded region: ± SEM for KO, centered at the mean (WT: N = 70; KO: N = 36; Kolmogorov–Smirnov test). (E) Cumulative probability distribution of mean field size calculated on a trial-by-trial basis. Only cells included in (D) are included. Gray shaded region: ± SEM for WT, centered at the mean; green shaded region: ± SEM for KO, centered at the mean (WT: N = 70; KO: N = 36; Kolmogorov–Smirnov test). (F) Mean field size of each neuron plotted against its mean phase precession slope. Black: WT; Green: KO (WT: N = 70; KO: N = 36; Kolmogorov–Smirnov test). (G) Schematic summarizing results. *p < 0.05.

independently, we compared the average per-trial field sizes between the WT and KO neurons. KO neurons had significantly larger per-trial field sizes than WTs (Figure 6E), although both were smaller than those calculated using the complete set of trials (Figure S5D). This result is consistent with the idea that our phase precession criteria selected for neurons with stronger spatial tuning. For both WT and KO neurons, field size and phase precession slope were highly correlated (Figure 6F) (Spearman's correlation: WT: Rho = 0.7754, $p = 1x10^{-10}$; KO: Rho = 0.7650, $p = 1x10^{-10}$). To determine the relative contributions of genotype, field size, and theta modulation strength to the difference in phase precession, we built a linear regression model, using these three variables as predictors (Table S1); field size and slope were log transformed to account for the non-linearities in these variables (Figure S6O and P). The model explained 28% of the variance in slope (adjusted $R^2 = 0.2784$) with field size emerging as the only significant positive predictor of phase precession ($\beta = 0.9191$, $p = 1.3433 \times 10^{-12}$). Thus, the reduction in phase precession observed in NPAS4 KO neurons is linked to the concomitant increase in place field size, suggesting a coupling between spatial representations and temporal precision of spiking that is perturbed when NPAS4-dependent regulation of inhibition is disrupted.

Discussion

NPAS4 orchestrates a reorganization of inhibitory inputs along the somatodendritic axis of CA1 pyramidal neurons, serving as a molecular link between a neuron's recent activity and targeted changes in inhibitory synapse composition. Here, we demonstrate that NPAS4-mediated reorganization of inhibition occurs in adult animals, not just in juveniles, suggesting that NPAS4 is important for tuning neuronal activity across the lifespan of the animal. Using a sparse knockout strategy and *in vivo* optotagging to differentiate between WT and KO neurons within awake, behaving animals, we identified several consequences of the loss of NPAS4, schematized in Figure 6G. First, we showed that NPAS4 KO neurons have more uniform firing across the track. Specifically, KO neurons exhibit lower firing rates within the neuron's place field and higher firing rates across the rest of the track. In addition to the degenerate representation of space, KO neuron place fields were less stable, shifting large distances over few trials. The temporal organization of spikes was also disrupted—KO neurons showed weaker theta coupling and exhibited shallower phase precession. Together, these findings reveal that NPAS4 expression has substantial and lasting consequences for the spatial precision and temporal organization of CA1 pyramidal neuron firing in adult mice.

Our experimental design provides insight into the cell-autonomous effects of behavioral experience on pyramidal neuron activity. By sparsely knocking out NPAS4 in adult mice, we reduce the likelihood of developmental or circuit-level compensations that could mask or exaggerate NPAS4-dependent phenotypes. While our manipulation is sparse, NPAS4 is knocked out for at least one month. Additional methodological innovation is needed to examine the more acute consequences of NPAS4 expression or deletion. Our use of electrophysiological recordings from intermingled WT and KO neurons enables precise measurement of spike timing relative to a shared local field potential (LFP)—a level of temporal resolution not achievable with calcium imaging[57,58]. This study advances our understanding of how an activity-dependent transcription factor shapes *in vivo* information encoding and creates a bridge between molecular and circuit-level biology.

Detailed knowledge of how NPAS4 changes inhibitory synaptic connectivity is an essential context for understanding the results in this study and reveals important future questions to be explored. NPAS4-dependent changes in CCK+ inhibition are necessary for the emergence of dendritic plasticity mechanisms[26]. We speculate that the increased dendritic inhibition observed in NPAS4 KO neurons suppresses burst firing and impairs dendritic plasticity—processes thought to stabilize place fields[46,59–69]. In contrast, reduced somatic inhibition may permit spikes to be generated when they should not be, leading to spurious out-of-field firing. Inhibition from CCK+ neurons onto CA1 pyramidal neurons has been shown to constrain place field size and increase stability[38]. Our findings support this role and extend it by linking activity-dependent expression of NPAS4 to the same spatial receptive field properties.

Beyond their role in shaping pyramidal neuron spatial receptive fields, CCK+ inhibitory neurons also contribute to the temporal organization of spiking through their influence on theta-modulated firing. *In vivo* recordings obtained from anesthetized rats[50] and awake behaving mice[40] have shown that CCK+ basket cell activity *itself* is theta-modulated, though the preferred phase of firing varies between paradigms. In principle[50,70], the rhythmicity of CCK+ basket cell firing imposes a window of opportunity for pyramidal neuron firing. Reduced CCK+ basket cell inhibition, as demonstrated in NPAS4 KO neurons[22], likely broadens this window thereby contributing to the diminished theta coupling observed in this study. While CCK+ inhibitory neurons have not been directly linked to phase precession, activation of CB1 receptors (found exclusively on CCK+ inhibitory neurons in the hippocampus) has been shown to disrupt phase precession[71,72]. We observe a clear disruption of this temporal coding property in NPAS4 KO neurons. Notably, phase precession slope was significantly correlated with place field size in our dataset—a relationship that also emerged as a key predictor in our regression model. Although others have reported similar correlations, the mechanistic link between field size and precession slope remains unresolved: does one drive the other, or do both arise from a shared upstream process? A major challenge for the field will be to develop strategies that disentangle these interdependent coding features and clarify how distinct forms of inhibition interact to shape them. Nevertheless, our findings demonstrate that the distribution of place field sizes and phase precession slopes are shifted in NPAS4 KO neurons, suggesting a shared dependence on NPAS4-mediated inhibitory synapse organization.

The activity of CCK+ inhibitory neurons is strongly modulated by behavioral state, suggesting that their influence on pyramidal neuron output may be particularly important during transitions in network dynamics. For example, CCK+ inhibitory neurons increase their firing during shifts from locomotion to immobility[73,74], and are particularly recruited during hippocampal ripples in NREM sleep[40]. Based on this, NPAS4 may be instrumental in suppressing pyramidal neuron firing during periods of rest and preventing indiscriminate recruitment into ripple-delimited replay events. While our study focused on periods of active exploration, future work examining how NPAS4 shapes CA1 activity during transitions to immobility or during specific stages of sleep, is likely to be especially relevant.

Finally, there are many activity-dependent transcription factors, in addition to NPAS4, that are expressed in neurons. Single-cell transcriptomics show us that the expression of these transcription factors often overlaps. For example, NPAS4+ neurons are often also Fos+. Yet, these two transcription factors drive different mutually-exclusive synaptic phenotypes, regulating somatic inhibition from CCK+ or PV+ basket cells, respectively[22,75]. Moreover, there is recent evidence that Fos also shapes spatial representations in CA1 pyramidal neurons, with high Fos expression correlating with larger, more stable place fields[16]. To understand the rich complexity of activity-dependent gene regulation, future studies that closely examine the synergistic, antagonistic, or mutually exclusive actions of different activity-dependent transcription factors are needed.

Methods

Mice

All experiments were conducted in accordance with National Institutes of Health (NIH) guidelines and following the approval of our protocol by UC San Diego's Institutional Animal Care and Use Committee (IACUC). An *Npas4*$^{fl/fl}$[5] animal line was used for acute slice electrophysiology experiments and an *Npas4*$^{fl/fl}$:Ai32 (Ai32 *RRID:IMSR_JAX:012569*) animal line was used for NPAS4 immunohistochemistry (IHC) and all *in vivo* electrophysiology experiments. Only male mice were used for the sparse *in vivo* experiments. All electrophysiology experiments were performed on adult animals (P70-P200) that were housed long-term in enriched environments. The enriched environment consisted of a running wheel, toys, wooden blocks, and other objects of various shapes, colors, and textures. To maintain novelty, toys were replaced every two days. For all electrophysiology experiments, mice were kept in the vivarium on a reverse 12-hour light-dark cycle and were single-housed.

NPAS4 Immunohistochemistry

For NPAS4 staining in enriched animals, adult mice (P70-P200) housed in a normal light-dark cycle were removed from the vivarium and left in a dark, empty room for two hours prior to the experiment. Half of the mice were then placed into an enriched environment (EE) for 90 minutes. In a separate set of experiments, additional mice received an intraperitoneal injection of kainic acid (KA; 2.5 mg/kg) and were placed in a large rat cage for 90 minutes. All KA-injected mice exhibited clear behavioral seizures during this period. The other half were left in their home cages for standard environment (SE) control. EE consisted of a large (2x2 ft) cardboard box with colorful patterns taped to the walls; two running wheels; plastic toys of various sizes, shapes, and colors; and wooden blocks. Mice were monitored for the full 90 minutes and continued to engage in the environment and actively explore for the majority of the enriched exposure. At the end of 90 minutes, mice from EE and SE were immediately anesthetized in isoflurane. The brains were extracted, the hippocampi dissected, and drop-fixed in 4% PFA for 2 hours. After 2 hours, the dissected hippocampi were rinsed in three ten-minute washes in 1X phosphate-buffered saline (PBS) before being moved to a 30% sucrose solution. The hippocampi were left in 30% sucrose overnight or until they had sunk to the bottom. The hippocampi were then frozen in OCT (optimal cutting temperature) compound and sectioned along the dorsoventral axis using a cryostat. Sections from the dorsal hippocampi were selected and blocked overnight in 10% goat serum/0.25% triton-X in PBS. Primary antibody solutions were applied to the slides and consisted of 1% goat serum, 0.25% triton-X, primary antibody against NPAS4 (1:500; RbαNPAS4; [5], and primary antibody against NeuN (1:1000; GPαNeuN; Synaptic Systems *RRID:AB_2619988*) in 1X PBS. The primary antibody solution was left for 48 hours at which point the slides were rinsed with three 10-minute washes of 1X PBS. Secondary antibody solutions were applied and consisted of 1% goat serum, 0.25% triton-X, Alexa 568 secondary antibody (1:1000; GtαRb; ThermoFisher; *RRID:AB_10563566*), and Alexa 647 secondary antibody (1:1000; GtαGP; ThermoFisher; *RRID:AB_2535867*) in 1X PBS. The secondary solution was left for 24 hours at which point the slides were rinsed with three 10-minute washes of 1X PBS. Slides were cover slipped using Fluoromount with DAPI and imaged at 60X using a confocal microscope. Images were acquired on an Olympus Fluoview 1000 confocal microscope (× 60/1.42 [oil] plan-apochromat objectives; UC San Diego School of Medicine Microscopy Core).

Image Quantification

To quantify the number of neurons expressing NPAS4 in the CA1 pyramidal cell layer, we manually counted the number of cells somatically expressing NPAS4 and divided by the total number of cells in the pyramidal cell layer (NeuN+). We used the same levels for all images and only counted cells as NPAS4+ if we observed NPAS4 signal in at least 50% of the soma as identified using our NeuN signal.

Viruses

For all sparse infection experiments (*ex vivo* and *in vivo* electrophysiology), an adeno-associated virus (AAV) expressing Cre-GFP was used (pENN.AAV.CamKII.HI.GFP-Cre.WPRE.SV40 AAV9; Addgene Item ID:105551-AAV9). To achieve a sparse infection, the virus was diluted 1:3 or 1:4 with sterile saline just before injection.

AAV Injections

All surgeries were performed in accordance with (NIH) guidelines and following the approval of our protocol by UC San Diego's IACUC. Stereotaxic viral injection surgeries were performed on adult animals (P70). Animals were injected with flunixin (2.5 mg/kg) subcutaneously pre-operatively and post-operatively every 12 hours for 72 hours. Animals were anesthetized with isoflurane for the duration of the surgery (1.5%-2% isoflurane vaporized in oxygen) and body temperature was maintained at 37° C using a delta phase pad. Following induction of anesthesia, the mice were placed in a stereotaxic apparatus, the fur covering the scalp was shaved cleanly, and the scalp was cleaned with three iterations of betadine and 70% ethanol. An incision along the

midline was made to expose the skull so that bregma and lambda could be observed. For both *ex vivo* (targeting medial CA1) and *in vivo* (targeting dorsal CA1) electrophysiology experiments the distance between bregma and lambda was used to scale the anterior-posterior (AP) coordinates.

For subsequent *ex vivo* experiments two burr holes were drilled bilaterally (four in total) above medial (along the dorsoventral axis) CA1. AP coordinates were calculated using an equation derived from successfully targeted surgeries. The equations for the AP coordinates were AP = (-2.30/3.14)*bregma lambda distance and AP = (-2.60/3.14)*bregma lambda distance. The medial-lateral (ML) coordinates were ±3.30 mm and the dorsal-ventral (DV) coordinates (three injections per burr hole) were -1.40, -2.50, and -3.60. For subsequent experiments in freely behaving mice, one burr hole was drilled above dorsal CA1 in the right hemisphere only. The equations for the AP coordinates were AP = (-1.44/3.14)*bregma lambda distance. The ML coordinates were ML=1.45 to 1.55 mm and the DV coordinates were DV=1.45 to 1.55 mm.

At each injection site virus was injected (*ex vivo:* 150 nL at each injection site; freely behaving: 300 nL; 100 nL/min) using a Hamilton syringe attached to a Micro4 MicroSyringe Pump Controller (World Precision Instruments). Three minutes post-injection, the needle was retracted, the scalp sutured, and the mouse recovered at 37° C before being moved to a new home cage in which it was individually housed for the duration of the experiments.

Acute Slice Preparation

Transverse hippocampal slices were prepared from *Npas4*$^{fl/fl}$ mice (P176-P184) at least three months after stereotaxic injection of AAV.Cre-GFP into CA1. Animals were anesthetized briefly by inhaled isoflurane and decapitated. Blocking cuts were made to isolate the portion of the cerebral hemispheres containing the hippocampus and slice preparation was prepared as described previously [22]. Specifically, hemispheres were mounted on a Leica VT1000S vibratome and bathed in NMDG-HEPES recovery solution (NMDG 93 mM, HCl ~93 mM, KCl 2.5 mM, NaH2PO4 1.2 mM, NaCO3 30mM, HEPES 20mM, glucose 13 mM, NAC 12mM, sodium ascorbate 5mM, thiourea 2mM, sodium pyruvate 3mM, MgSO4 10mM, CaCl2 0.5mM, 300-310 mOsm, pH 7.3-7.4 with HCl, saturated with 95% O2/5% CO2). After cutting, sections were transferred to 34° NMDG-HEPES recovery solution and sodium was spiked in over 30 minutes as previously described [76]. Slices were then transferred to modified HEPES holding ACSF [76] (NaCl 92mM, KCl 2.5mM, NaH2PO4 1.2 mM, NaHCO3 30mM, HEPES 20mM, glucose 13 mM, NAC 12mM, sodium ascorbate 5mM, thiourea 2mM, sodium pyruvate 3mM, MgSO4 2mM, CaCl2 2mM, 300-310 mOsm, pH 7.3-7.4 with NaOH, saturated with 95% O2/5% CO2) where they were recovered for 1 hour and then maintained for the remainder of the day (~6 hr).

Ex Vivo Electrophysiology and Pharmacology

Infection density varied with distance from the injection site and slices were selected in which ~10–50% of neurons were seen to be infected on the basis of GFP expression as assessed by eye before recordings. For paired whole-cell patch-clamp recordings, slices were transferred to the recording chamber with ACSF (127 NaCl, 25 NaHCO3, 1.25 Na2HPO4, 2.5 KCl, 2 CaCl2, 1 MgCl2, 25 glucose, saturated with 95% O2/5% CO2). Whole-cell patch clamp recordings were acquired simultaneously from neighboring Cre+ and Cre- pyramidal neurons in superficial CA1 and extracellular stimulation of local axons within specific lamina (SP or SR) of the hippocampus was delivered by current injection through a theta glass stimulating electrode that was placed in the center of the relevant layer (along the radial axis of CA1) and within 100-300 μm laterally of the patched pair. eIPSCs were pharmacologically isolated with CPP (10 μM) and NBQX (10 μM) in all experiments. Patch pipettes (open pipette resistance 2–4 MΩ) were filled with an internal solution containing (in mM) 147 CsCl, 5 Na2-phosphocreatine, 10 HEPES, 2 MgATP, 0.3 Na2GTP and 2 EGTA (pH=7.3, osmolarity=300 mOsm) and supplemented with QX-314 (5 mM). All recordings were performed at 31° C.

Electrophysiology data were acquired using ScanImage software [77] and a Multiclamp 700B amplifier. Data were sampled at 10 kHz and filtered at 6 kHz. Off-line data analysis was performed using NeuroMatic [78]. Experiments were discarded if the holding current for pyramidal cells with

CsCl-based internal solution was greater than −500 pA, if the series resistance was greater than 25 MΩ, or if the series resistance differed by more than 25% between the two cells. Individual traces were examined and if either recording contained spontaneous events that obscured the evoked IPSC then both the Cre+ and Cre- sweeps were excluded and average traces were created from technical replicates. Ratio-paired t-tests were performed comparing Cre+ to neighboring Cre-eIPSC amplitudes.

Optetrode Fabrication

Optetrodes were fabricated following previously published designs with slight modifications [79]. Briefly, the tetrodes used in the optetrodes were prepared by braiding four platinum-iridium wires (0.0007 mm diameter; California Fine Wire Company) together and applying heat to bind the wires together. Four of these tetrodes were then loaded into a 16-channel electronic interface board (EIB-18, Neuralynx) and pinned in place with gold pins to ensure stable connection with the EIB. An optic fiber (200 µm diameter; Doric Lenses; product code: MFP_200/240/900-0.22_#.#_SMA_ZF1.25(F)) was inserted through the middle of the four tetrodes such that the tetrodes evenly surrounded the optic fiber. The tetrodes were secured to the tip of the optic fiber using a small amount of glue before being plated with a platinum-iridium solution to achieve impedances between 100 and 200 MΩ.

Optetrode Implantation

All surgeries were performed in accordance with (NIH) guidelines and following the approval of our protocol by UC San Diego's IACUC. Optetrode implantation surgeries were performed on mice who had recovered well from the injection surgery (5-14 days between surgeries; 8 adult male mice). Animals were injected with a slow-release buprenorphine (0.02 mg/kg) subcutaneously pre-operatively which provided analgesia for 2-4 days post-op. Animals were anesthetized with isoflurane for the duration of the surgery (1.5%-2% isoflurane vaporized in oxygen) and body temperature was maintained at 37° C. Following three repetitions of cleaning the skin with betadine and 70% ethanol, the previous incision site was reopened and the skull exposed. Four stainless steel screws were anchored into the skull to provide stabilization and support for the implant. The same coordinates used for viral injection were used for the site of the craniotomy while a ground screw was inserted at the same AP coordinates in the left hemisphere. Following a craniotomy and durotomy, a stereotaxic frame was used to slowly lower the tetrodes into the brain. The tetrodes were lowered to a depth of ~0.5 mm and the entire craniotomy was covered with gel (sodium alginate cured with calcium chloride) to protect any exposed brain and tetrode wires. The entire skull was then covered in dental cement to firmly secure the optetrode to the skull and anchor screws. Following surgery, the mice recovered in their home cage over a heating pad until awake and moving.

Handling and Behavior

Once mice had recovered from the optetrode implant surgery (minimum of five days) we began habituation and food deprivation. Food deprivation was slowly introduced over 4-7 days until mice reached ~90% of their full body weight. For the first three days of habituation, mice were brought to the experimental room and handled by the experimenter for 5-15 minutes. On days 4-6, 20-30 chocolate sprinkles (the reward used in the task) were randomly placed on the track and mice were allowed to forage for 15 minutes or until all the chocolate sprinkles were gone. Once mice ate 80% of the chocolate sprinkles within 15 minutes, we began task training.

The task consisted of a figure-8 maze that had the central arm blocked off so that mice could only run along the outer rectangular track. To begin with, mice were blocked into one arm of the track. Once data acquisition had begun, one of the blocks was removed (alternated each day) and the mouse was allowed to run in one direction around the track, receiving a chocolate sprinkle at the front center of the track, opposite of the starting point, for each trial. The second block was removed to allow running of full laps. At the end of each epoch of trials (5 trials for training and 10 for recordings), a block was placed just after the reward zone forcing the mouse to turn around

and run the other direction for 10 trials. A recording session ended when the mouse had run 80 trials or for 30 min., whichever occurred first. If the mouse was unable to run 60 trials in 30 minutes, the session was excluded from analysis.

Before and after each track recording session, home cage recordings were obtained. Home cage recordings took place in the animal's cage which was placed just to the side of the track and in view of the camera. If units were recorded that day, we also obtained an optostimulation recording in the home cage at the end of the session.

Electrophysiology Recordings in Behavior

After the animals had recovered from the optetrode implant surgery (minimum of five days), the tetrodes were slowly advanced over the course of several days until the hippocampus was reached. CA1 was identified by the presence of strong theta oscillations in the LFP, ripples, and the presence of well-isolated clusters. Just before reaching CA1 and throughout the rest of the experiment, the tetrodes were lowered 14-28 μm per day to ensure that the recordings were stable and that new cells were recorded on a daily basis. Once all tetrodes left the CA1 pyramidal cell layer and had clearly entered stratum radiatum as reflected by inversion of ripples and lack of excitatory cell activity, no further recording sessions were performed.

To perform the recordings, the microdrive was connected to a digital Neuralynx recording system through a multichannel headstage preamplifier. The headstage and preamplifier were supported with elastics to assist the mouse in holding the weight. The LFP was band-pass filtered (0.1 to 8,000 Hz) and a threshold of 45-60 μV applied to isolate putative spikes. The LFP was continuously sampled at 32,000 Hz from one of the wires on each tetrode.

Position Tracking

To track the animals' position, we used a previously published, open access method [80]. An Arduino (Mega 2560) was programmed to deliver a synchronizing pulse that consisted of 1 msec on, 1 msec off, followed by a series of pulses that counted up from 0 in binary. This pulse was fed into one of the CSC channels of the Neuralynx system and was also fed into the audio output of a camcorder (Sony HDR-CX380) that was used to obtain video of the animal's position. The animal's position was estimated to a high degree of certainty using LEDs that were mounted on the headstage preamplifier. If the position could not be obtained (primarily occurring when the preamplifier cord moved between one of the LEDs and the camera), a value of NaN was assigned. Using the pulse on the audio channel and the pulse on the CSC channel, a custom MATLAB workflow was generated allowing us to synchronize the animal's XY position with the Neuralynx recordings. We validated the accuracy of this procedure as described in the initial publication[80].

Optotagging

At the end of each recording day, a 20–30-minute optotagging session was conducted. A laser (Opto Engine P/N:MBL-III-473-100mW) was used to deliver 473 nm wavelength light through a patch cable (SMA, 200 μm core, NA 0.63, Thor Labs) to the optic fiber in the optetrode assembly. Before the recording began, the light power was carefully set so that a small but discernible response could be observed occasionally in the LFP but no population spike was elicited (typically ~0.3mW, Figure S2A). The population spike cluster was easily discernible by eye when it did occur as the amplitude was large and roughly equivalent for all the channels of a given tetrode (Figure S2B). For all optotagging experiments, light was delivered at 0.5 Hz; light-on for 10 msec.

For the high-power validation experiments, we waited until the end of the normal optotagging session then increased the laser power such that a population spike was noticeable on all four channels. During the high-power stimulation, we observed a clear response in the LFP and population spikes on all tetrodes on which units had been recorded that day (Figures S2B and S2D). In some cases, some of the clusters nearly disappeared suggesting that these were opto-tagged cells that contributed to the population spike. Following stimulation, all previously identified clusters reappeared. While we cannot directly prove that the unit identity was the same before and after light stimulation, we observed that the re-emerging clusters maintained

consistent waveform features — including peak amplitude, energy, and peak-to-valley ratio — and remained in the same region of cluster space as before stimulation. These observations support the interpretation that the same neurons were recovered after high-power stimulation.

Spike Sorting and Cluster Quality

The spike sorting software MClust (MATLAB 2009b, Redish Lab; *https://redishlab.umn.edu/mclust*) was used for spike sorting. Cluster cutting was performed manually using two-dimensional projections of the parameter space. For our cluster cutting parameters, we used amplitude, peak-valley ratio, and waveform energy. In most cases, the cluster cutting boundaries were originally established in the track recordings then applied to the home cage and optotagging recordings. To be included in analysis, all clusters had to appear qualitatively well-separated. Cluster quality was quantitatively assessed using the L-Ratio and Mahalanobis distance for units recorded on tetrodes with all four working channels (Figure S2G and S2H).

Unit Classification

During cluster cutting, we immediately excluded clusters if they had a mean firing rate above 5 Hz as this would suggest that either this was an interneuron or it was an overlapping cluster of two cells. Although others have used other metrics (such as the shape of the waveform or the burstiness of the cell) to isolate interneurons we did not do that in this study for two reasons. First, the interneurons that are known to be involved in the NPAS4 phenotype are CCK basket cells[22] which are regular-spiking cells that do not have a narrow waveform. Second, although CCK basket cells are not bursty and can be separated from pyramidal neurons using a burst index, we observed differences in bursting as part of the NPAS4 phenotype and could not use this as an exclusion metric. For these reasons, it is possible that our WT population may contain a small subset of interneurons[47]. Importantly, if this were the case, given what we know about these interneurons, it would obscure the differences between WT and KO neurons that we report here. We expect that our KO population is entirely excitatory since Cre is expressed under the CamKII promoter.

Next, the remaining population of cells was sorted into putative WT cells, KO cells, or excluded cells based on their optotagged response. For each cell, we separated the spikes that occurred during the optostimulation session into trials (duration of 2 s per trial). We aligned spikes according to when the light pulse was delivered and calculated the peristimulus time histogram (PSTH) using bin sizes of 1 ms. Using the PSTHs, the opto-response was defined as the maximum response when the light was off subtracted from the maximum response when the light was on. If a cell appeared ambiguous (i.e. was low firing or had an opto-response of 1) we excluded it from all analyses in this paper. Cells that had an opto-response greater than 1 (i.e. in which the maximum response in the PSTH during light-on was greater than the maximum response in the PSTH during light-off) were considered KO cells while cells with an opto-response less than 1 were considered WT cells.

Perfusion and Tissue Processing in Behavioral animals

At the end of the experiment, all mice were anesthetized with a mixture of ketamine and xylazine (100 mg/kg ketamine, 10 mg/kg xylazine) and were perfused with ~40mL of saline followed by ~40mL of 4% paraformaldehyde (PFA). The tetrodes were carefully raised out of the skull and the brains were extracted and drop-fixed for an additional 24-48 hours in 4% PFA. The brains were rinsed in three 10-min washes with 1X PBS and left in a 30% sucrose solution for 24 to 48 hours or until the brains had sunk. A microtome was used to section the brains into 50 μm coronal sections which were then mounted onto slides, stained with DAPI, and coverslipped.

Histology and Identification of Tetrode Locations in Behavioral Animals

All coronal sections spanning the dorsal hippocampus were imaged using a Keyence microscopy system. Images obtained at 2X magnification were used to confirm that the infection extended throughout dorsal hippocampus. Stitched 10X images were used to confirm the location of the tetrode tracts within the CA1 pyramidal cell layer. Finally, 60X images were obtained anterior to, posterior to, medial to, and lateral to the site of the tetrode implants to quantify the percentage of knockout cells (% GFP+; Figures S1, S2I, and S2J). All animals used in this study had infection that was primarily localized to CA1 (some expression in CA2 and cortex) and in which the implant site fully overlapped with the infection. Tetrode locations were primarily located medially in CA1 along the proximodistal axis with a slight skew towards distal CA1.

Calculation of ISI Histograms and Burst Index

The interspike intervals (ISIs) were calculated by finding the difference in timing between each spike and the one after it. The ISIs were then binned into 10 ms bins and the burst index was calculated by taking the number of spikes that occurred at ISIs less than 10 ms and normalizing by the total number of spikes for that cell.

Quantifying Firing Rates and Spatial Tuning

For each session, the velocity was calculated by averaging over 1 s using 0.1 s sliding windows. Only spikes during periods of running (velocity ≥ 2 cm/sec) were used for analysis. For each cell, we divided spikes into those that occurred when the animal was running clockwise and those that occurred when the animal was running counterclockwise, analyzing each set of spikes separately for all analyses. The mean and max. firing rates were obtained from the spatial maps and used to define the cut-off for low-firing cells. Cells with a mean firing rate < 0.1 Hz and a max firing rate < 1 Hz were excluded from analysis. Note that in a control analyses we excluded all cells with a mean firing rate < 0.5 Hz and a max firing rate < 5 Hz and the spatial tuning results still held. The track was linearized for each trial such that the reward zone was always at 0 cm and the center of the left and right arm were always 66 cm and 198 cm respectively.The animal's position was binned into 4 cm bins, and the spike rate within each bin was used to construct raw linearized rate maps. These maps were then smoothed using a five-point symmetric weighted filter with weights [0.02, 0.10, 0.16, 0.10, 0.02], effectively approximating a Gaussian kernel. Bins in which the position could not be computed or the velocity was below the threshold were set to 'NaN' and appear blank or gray in the rate maps.

For the trial-averaged spatial tuning in Figure 2 , we averaged across trials and used the trial-averaged maps to calculate the spatial tuning metrics (place field number, place field size, spatial information, and sparsity). To calculate the spatial tuning on individual trials, we first analyzed each trial individually and then used the average of all trial-wise values for each cell to statistically compare WT and KO populations. For analyses that depended on the identification of place fields (number of fields, size of fields, and all in-field/out-of-field analysis throughout the paper) a field was defined as the set of contiguous bins with firing rates above 10% of the max and in which one bin was greater than 50% of the max. For the average place field analysis, three neurons with very large place fields spanning the majority of the track were excluded. These units were suspected to be interneurons based on their atypically broad spatial tuning. Importantly, the statistical outcomes of the analysis were unchanged when these neurons were included. The signal-to-noise was the average in-field firing rate divided by the average out- of-field firing rate. The spatial information and sparsity were calculated as previously described[34] using the equations

$$\text{spatial information} = \sum_{i=1}^{N} p_i \frac{\lambda_i}{\lambda} \log_2 \frac{\lambda_i}{\lambda}$$

and

$$\text{sparsity} = \frac{(\Sigma p_i \lambda_i)^2}{\Sigma p_i \lambda_i^2}$$

where $i = 1, \ldots, N$ represents the spatial bins, p is the occupancy probability of bin i, λ_i is the mean firing rate for bin i, and λ is the overall mean firing rate for the cell.

Stability of Firing Patterns Across Epochs, Shuffle Control, and Calculation of Place Field Shifts and Difference Maps

For all correlation analyses we used the Pearson's correlation coefficient (PCC) on the trial-averaged rate maps. To compare firing in the clockwise and counterclockwise directions, we averaged the trials for each direction and calculated the PCC between them. To calculate the stability in spatial firing patterns across epochs we first averaged the trials for each epoch (set of 10 trials). We then calculated the PCC between each epoch and the subsequent epoch. For the shuffle control, we randomly shifted the rate map for each trial in space, enforcing a criterion that the shift must be at least 10 cm. We then averaged the trials for each epoch and calculated the PCC as described for the non-shuffled data. We repeated the shuffle 100 times and used the average PCC values for each cell. When calculating the stability using only in-field or out-of-field bins we used the trial-averaged rate maps for the full session and labeled bins as in-field if they were within a place field or out-of-field if not. We then repeated the stability analysis separately on the in-field and out-of-field bins. For all correlation calculations, if any bin had a value of NaN, it was removed from both vectors in that correlation comparison. To quantify place field shifts, we measured the change in the location of the peak firing bin between consecutive epochs for each place field independently. A negative shift indicated movement of the field toward the entrance of the track, while a positive shift indicated movement toward the field exit. Neurons with a peak shift less than −1 bin were classified as shifting toward the field entrance, those with a shift greater than +1 bin were classified as shifting toward the field exit, and neurons with a shift between −1 and +1 bins were considered stable.

Firing rate difference maps between epochs were computed by subtracting the firing rate map of the earlier epoch from that of the later epoch for each neuron (e.g., E2-E1, E3-E2, E4-E3). Difference maps were aligned by the E1 peak and displayed in the same neuron order across all comparisons.

Analysis of the Local Field Potential (LFP) Using FOOOF (Fitting Oscillations and One-over-f)

Hippocampal LFP recordings from the last two track recording sessions containing units were analyzed across all animals. The LFP data was downsampled from 32 kHz to 1 kHz and preprocessed using the neurodsp package (*https://neurodsp-tools.github.io/neurodsp/*). This package was used to extract the frequency band of interest (0.1-100 Hz). Bandpass filtering was performed using a Butterworth filter provided through neurodsp (4th order filter, [0.1 - 100Hz]).

The FOOOF (Fitting Oscillations & One-Over F) package (*https://github.com/fooof-tools/fooof*) was used to analyze theta oscillations in the hippocampal LFP. This tool enables the characterization of neural oscillations by decomposing the power spectrum into a combination of periodic and aperiodic components. The theta frequency of interest was selected as 5-12 Hz. The FOOOF algorithm fits a model consisting of a combination of Gaussians to capture the periodic components (theta oscillations) and a smooth aperiodic function to describe the background activity. The parameterization process involved fitting the model to the power spectrum of each LFP recording. To quantify the power within the theta frequency band for each LFP recording, the power between 5-12 Hz was extracted and analyzed.

Theta Modulation and Phase Precession of Single Units

For each cell, the LFP corresponding to the tetrode on which the unit was recorded was filtered in the theta frequency range using a Butterworth filter with cut-off frequencies of 4 and 12 Hz. For each spike a unit emitted, the theta frequency was obtained. Using circular statistics, we obtained

the mean vector length and mean phase for each cell where 180° was the trough of theta and 0° was the peak. This same approach was used on spikes that occurred in-field/out-of-field and on spikes belonging to bursts/singles. For analyses separating bursts and single spikes, bursts were defined as spikes with interspike intervals (ISIs) less than 10 ms, and singles as spikes with ISIs greater than 10 ms.

For phase precession analyses, only in-field spikes were considered. For each trial, we plotted the theta phase of each in-field spike against the normalized position within the place field[37]. To account for the circular nature of phase data, we circularly shifted spike phases in 5° increments and computed the correlation between theta phase and spatial position at each step, identifying the shift that produced the maximum (most negative) correlation[54]. Using these optimally shifted phases, we fit a linear regression to describe the phase precession slope for each trial. To ensure sufficient data quality and reliable fits, we included only neurons with at least five in-field spikes per trial, a spatial span of at least three theta cycles, and a significant linear fit ($p < 0.05$). The median slope across trials was used to represent the overall phase precession for each neuron.

To assess the relationship between place field size and phase precession strength, we selected the trial with a slope closest to the median phase precession slope for each neuron. Place field size was log-transformed, resulting in an approximately linear relationship with phase precession slope. A simple linear regression was then performed, and we report the regression slope, R^2, and p-value. Theta modulation strength was defined using the mean vector length (MVL) as described above.

A multiple linear regression model was constructed using genotype, log-transformed place field size, and MVL as predictors of phase precession slope. Shuffling controls were performed by randomizing either spike phase or position within trials. Bootstrapping was used to test the robustness of slope estimates by randomly sampling neurons with replacement while maintaining the original sample size per genotype.

Statistical Analysis

Statistical analyses were performed as described in the figure legends. Non-parametric tests were used unless otherwise indicated. Analyses were performed in GraphPad Prism and MATLAB.

Use of generative AI tools

During the preparation of this work the authors used ChatGPT (OpenAI) to help revise and edit portions of the manuscript text for clarity and conciseness. No content was generated that affected the scientific results or conclusions. After using this tool/service, the authors reviewed and edited the content as needed and take full responsibility for the content of the published article.

Data availability

The datasets generated during this study will be deposited in a public repository (e.g., OSF) and made freely available upon publication. Custom analysis code is available at *https://github.com/Bloodgood-Lab/Payne-et-al/tree/main*, and will be further documented and archived prior to publication.

Supplemental Figures

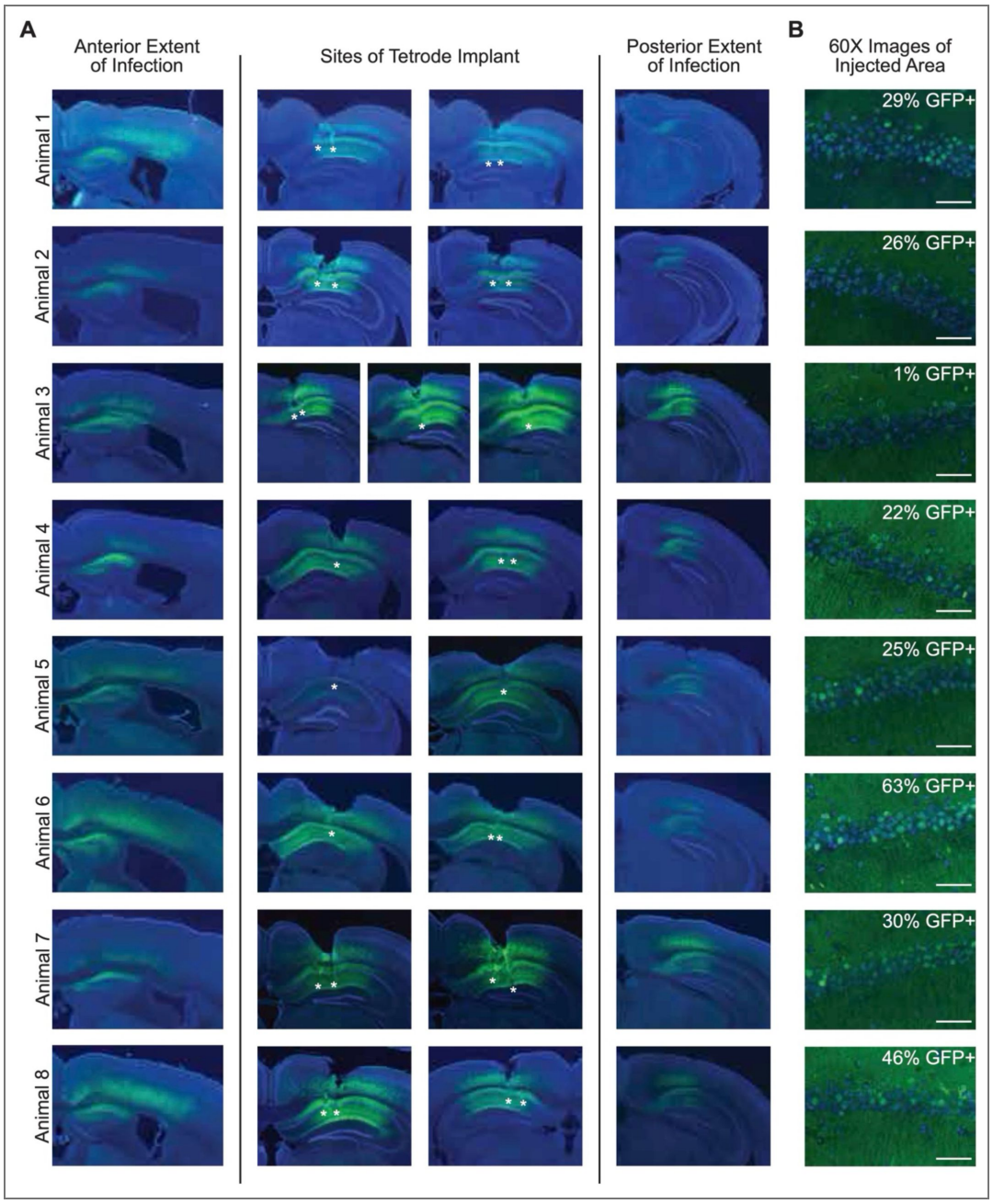

Supplemental Figure 1. Representative histology for all sparse-infection animals. (A) Left: Stitched 10X images showing the anterior extent of the infection. Middle: Site of optetrode implant in CA1, asterisks represent the end of the tetrode tracts. Not all tetrode tracts were able to be identified. Right: Stitched 10X images showing the posterior extent of the infection. (B) Representative 60X images near the site of implant showing sparse infection. Scale bar = 50 μm.

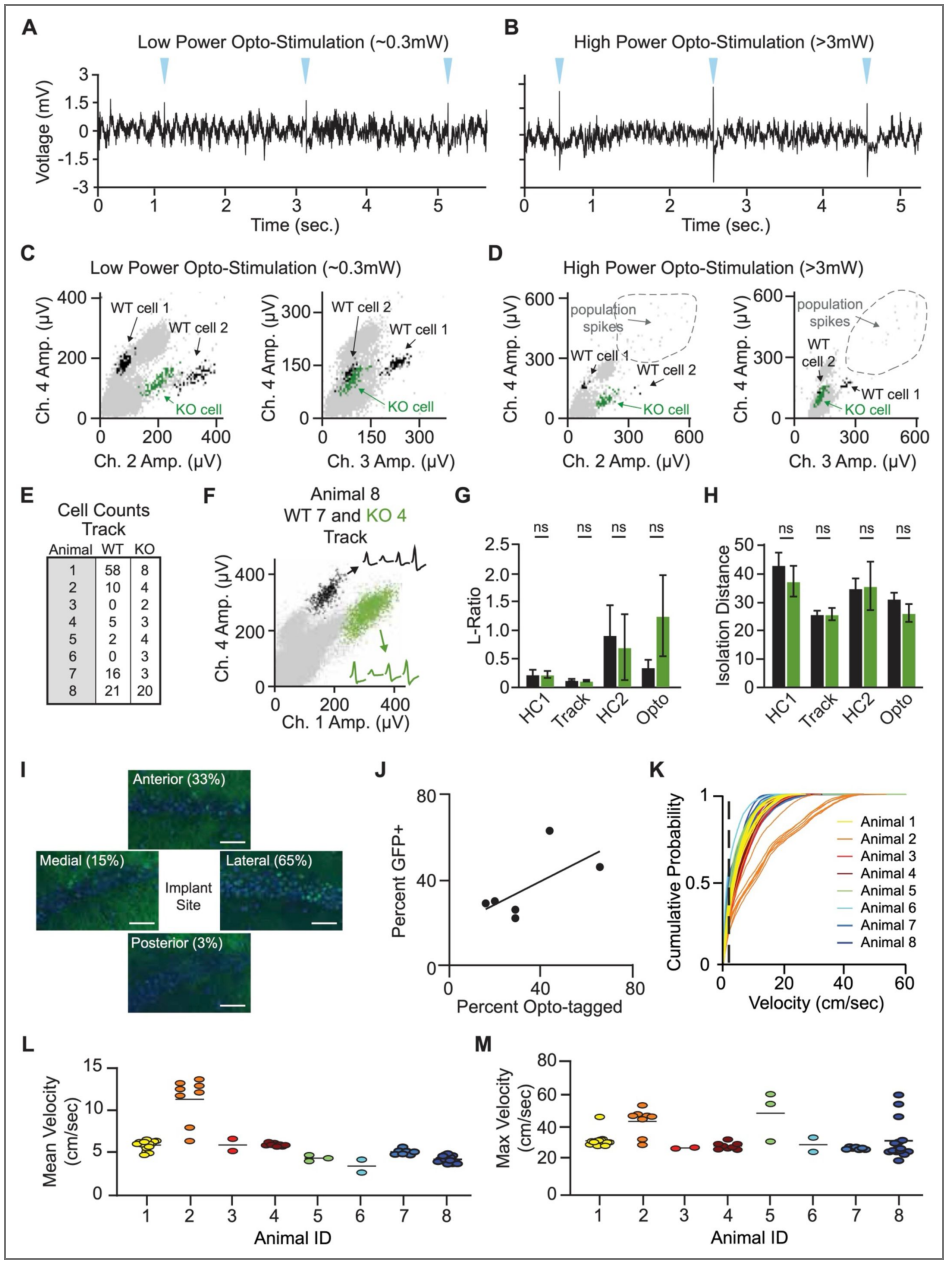

Supplemental Figure 2. Optical identification and functional characterization of NPAS4 KO neurons in vivo.

(A) Example of unfiltered LFP recording during light stimulation. Blue triangles = light delivery. (B) Example of unfiltered LFP recording during high-power light stimulation. (C) Example of cluster cutting for two WT neurons and a KO neuron during low-level light stimulation. Black dots: spikes from two WT neurons; green dots: spikes from one KO neuron. (D) Same neurons and cluster views as in (C) but for high-power stimulation. Dotted circle: putative population spikes. (E) WT and KO cell counts for each animal during track recordings. (F) Example of cluster cutting for a track recording showing a WT cell (black) and KO cell (green). Insets are average spike waveforms for each of the four tetrode channels for each neuron. (G) L-ratio for WT and KO cells for pre-track home cage (HC1), track, post-track home cage (HC2), and during optostimulation (HC1 WT N=70, KO N=34; track WT N=112, KO N=36; HC2 WT N=78, KO N=15; opto WT N=108, KO N=33; Kolmogorov–Smirnov test). (H) Isolation distance for WT and KO cells for HC1, track, HC2, and opto (HC1 WT N=71, KO N=36; track WT N=111, KO N=37; HC2 WT N=78, KO N=16; opto WT N=108 KO N=34; Kolmogorov–Smirnov test). (I) Example of how the percent infection is obtained from histology. 60X images taken anterior, posterior, medial, and lateral of the implant site. The percent infection per animal shown in (J) is an average of all four sites. Scale bar = 50 μm. (J) The percent of infected cells identified in histology plotted against the percent of optotagged cells identified *in vivo*. Line of best fit is shown. (K) Distribution of velocity for each session the sparse KO animals ran. (L) Mean velocity for all sparse KO animals. (M) Max velocity for all sparse KO animals. ns = not significant.

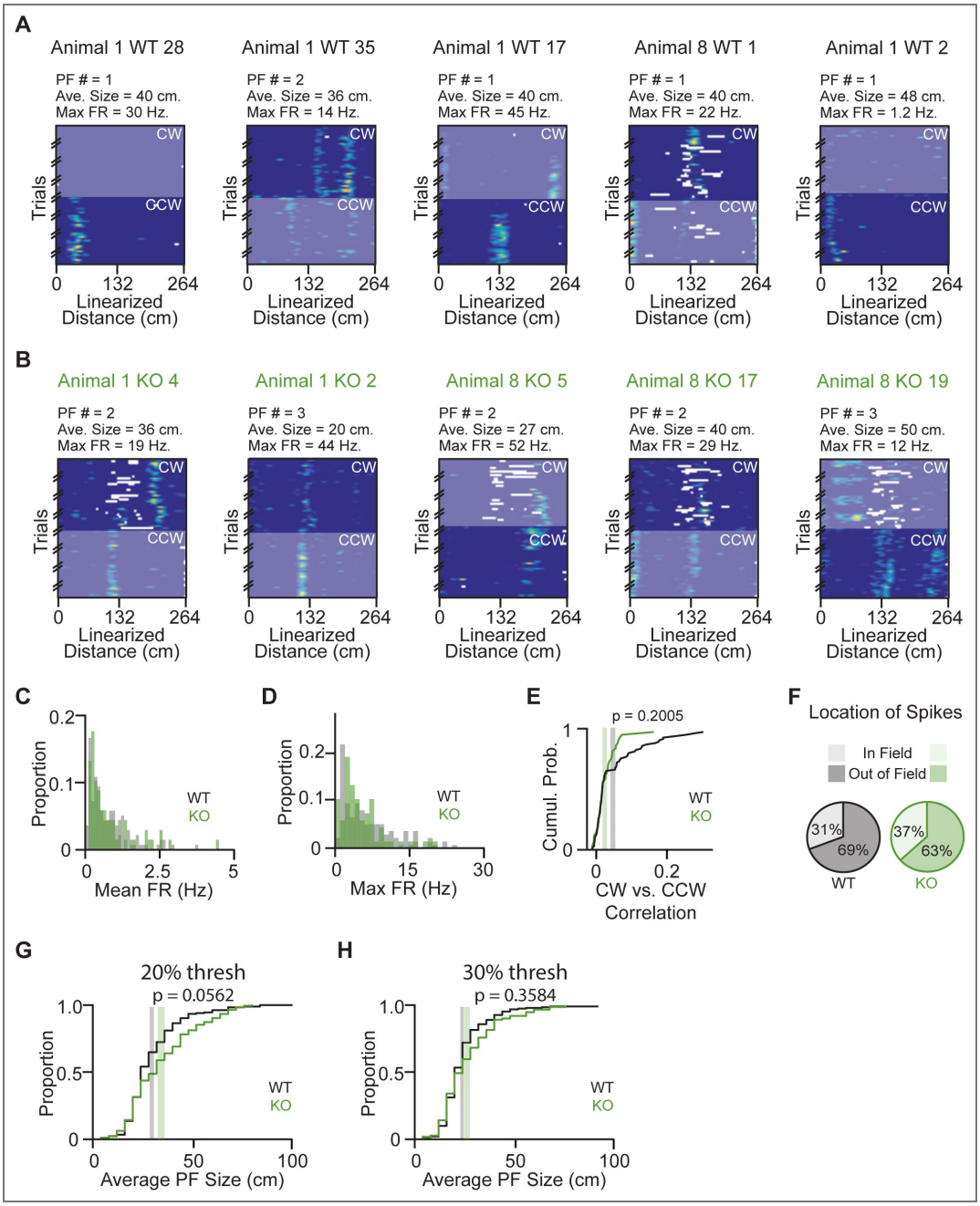

Supplemental Figure 3. Additional information on spatial firing rate properties for NPAS4 WT and KO neurons.

(A) Additional examples of rate maps from five WT cells. For each cell, both clockwise (CW) and counterclockwise (CCW) directions are shown; the direction not used for analysis is greyed out. The summary data shown above each rate map (Place Field Number [PF #], Average Size [Ave. Size], and Maximum Firing Rate [Max. FR]) corresponds to the analyzed direction only. (B) As in (A) but for KO cells. (C) Histogram of mean firing rate for all neurons (both low firing and high firing; WT: N = 224; KO: 94). (D) As in (C) but for the maximum firing rate. (E) Pearson's Correlation Coefficient (PCC) between the trial-averaged CW rate map for each neuron and the trial-averaged CCW rate map (WT: N = 138; KO: N = 68; Kolmogorov–Smirnov test). (F) The percentage of all spikes for all neurons that occurred in-field and out-of-field for WT and KO neurons (WT: N = 140; KO: N = 68; p = 0.21; chi-square goodness-of-fit test). (G) Average place field size as calculated in the main figure with the exception that the minimum threshold used was 20% of max firing instead of 10% of max firing (WT: N = 138; KO: N = 68; Wilcoxon rank sum test). (H) As in (G) but with a minimum threshold of 30% (WT: N = 138; KO: N = 68; Wilcoxon rank sum test).

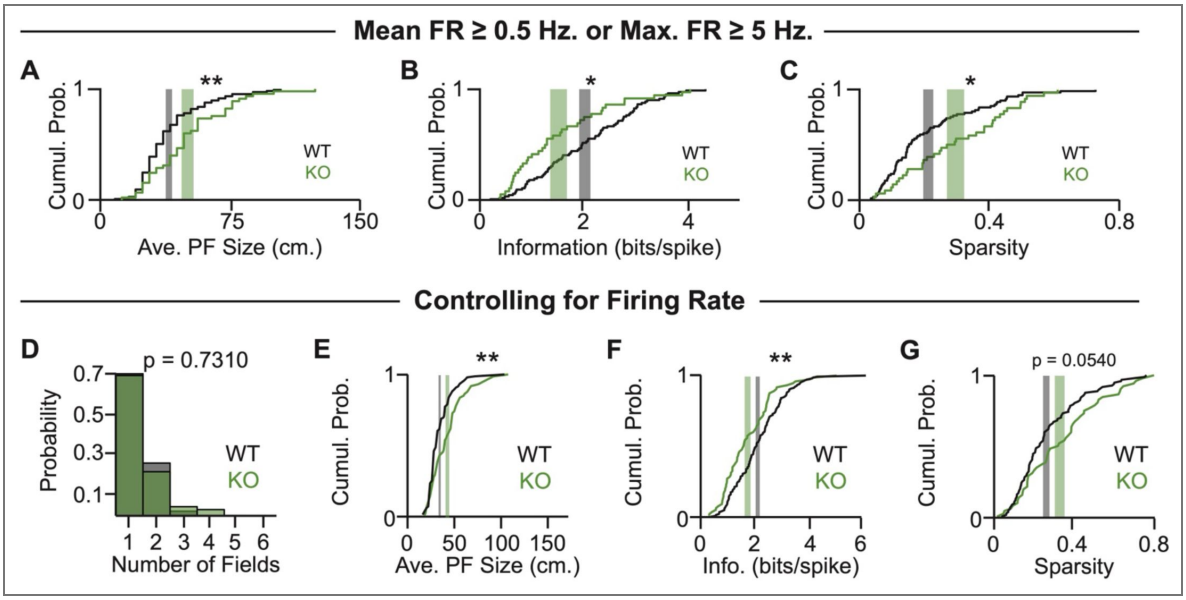

Supplemental Figure 4. Spatial deficits persist across firing rate thresholds, matched firing rates, and independent replication.

(A) Cumulative probability distribution of average place field size when only including neurons with mean firing rates > 0.5 Hz or max firing rates > 5 Hz. Gray shaded region: ± SEM for WT, centered at the mean; green shaded region: ± SEM for KO, centered at the mean (WT: N = 81; KO: N = 36; Kolmogorov–Smirnov test). (B) As in (A) but for spatial information. (C) As in (A) but for sparsity. (D) Histogram of the number of place fields per neuron when the number of spikes is the same across all neurons (WT: N = 138; KO: N = 68; Mann–Whitney test). (E) Cumulative probability distribution of average place field size when the number of spikes is the same across all neurons. Gray shaded region: ± SEM for WT, centered at the mean; green shaded region: ± SEM for KO, centered at the mean (WT: N = 81; KO: N = 36; Kolmogorov–Smirnov test). (F) As in (E) but for spatial information. (G) As in (E) but for sparsity. *p < 0.05; **p < 0.01.

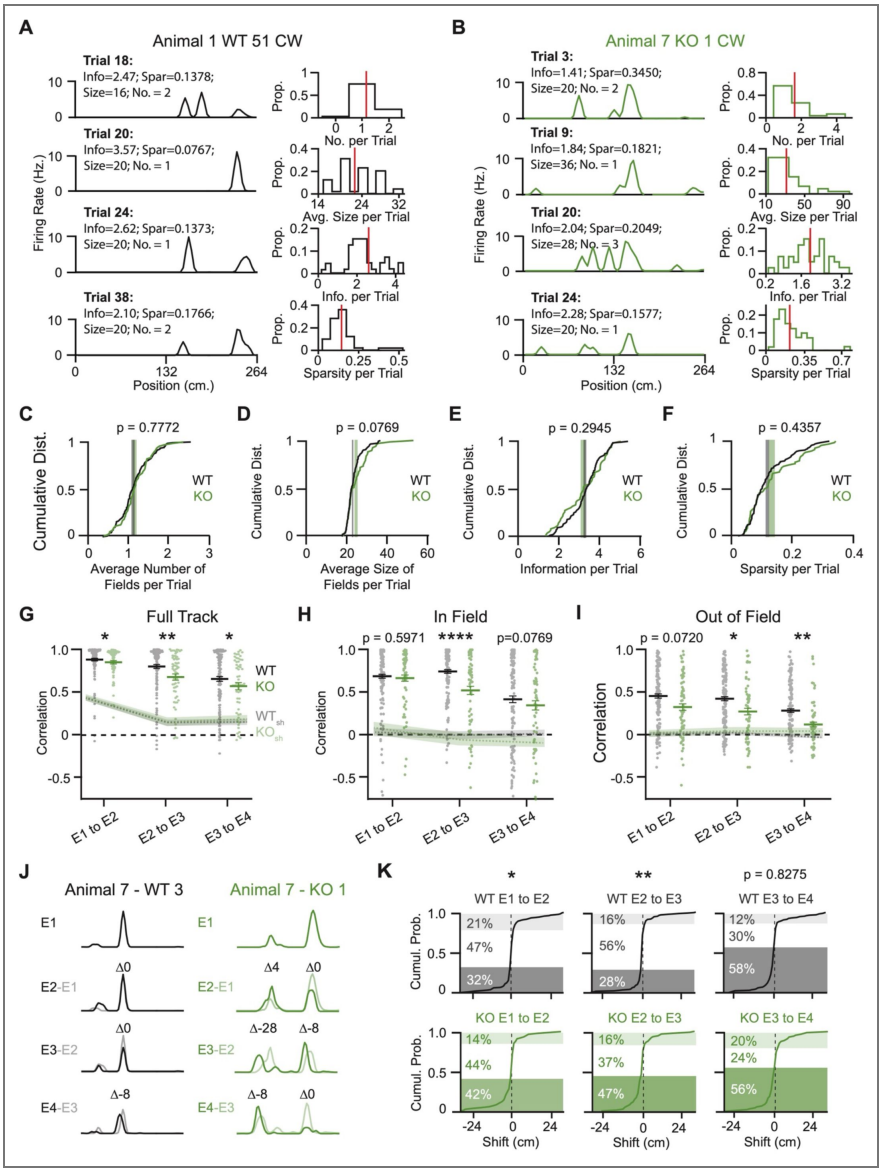

Supplemental Figure 5. NPAS4 stability deficits are the result of spurious out-of-field firing and shifts in the place field towards field entrance.

(A) Left: Four representative trials for a WT example cell. The number of fields, size, information, and sparsity are calculated independently for each trial. Right: For the same example cell, histograms for (top to bottom) the number of place fields, the average size of the place fields, the information, and the sparsity calculated for each trial independently and shown for all trials. Red line depicts the average. (B) As in (A) but for an example KO cell. (C) Median number of place fields per neuron. The number of fields was computed independently for each trial, then the median value was calculated for each neuron (WT N=140, KO N=68; Mann-Whitney test). (D) As in (C) but for the average place field size (WT N=140, KO N=68; Kolmogorov–Smirnov test). (E) As in (C) but for the spatial information (WT N=140, KO N=68; Kolmogorov–Smirnov test). (F) As in (C) but for the sparsity (WT N=140, KO N=68; Kolmogorov–Smirnov test). (G) Correlation between sequential sets of epochs (E1 to E2, E2 to E3, and E3 to E4) for all bins across the track. Gray dots: WT neurons; green dots: KO neurons; dotted gray: shuffled WT; dotted green: shuffled KO (WT N=140, KO N=68; Kolmogorov–Smirnov test). (H) As in (G) but for only the in-field bins for each neuron (WT N=140, KO N=68; Kolmogorov–Smirnov test). (I) As in (G) but for only the out-of-field bins for each neuron (WT N=140, KO N=68; Kolmogorov–Smirnov test). (J) Example trial-averaged rate maps for each epoch from one WT (left) and one KO (right) neuron to show shift calculation. Shift (denoted as Δ) is negative when the field shifts towards field entrance and positive when it shifts towards field exit. (K) Shift values for WT (top) and KO (bottom) across sequential sets of epochs (E2-E1, E3-E2, E4-E3). Dark shaded regions: fields with shift less than -1; unshaded regions: fields with shift between -1 and 1; light shaded regions: fields with shift greater than 1. Significance indicates comparisons between WT and KO (WT: N = 176 fields from 138 neurons; KO: N = 91 fields from 68 neurons). *p < 0.05; **p < 0.01; ****p < 0.0001.

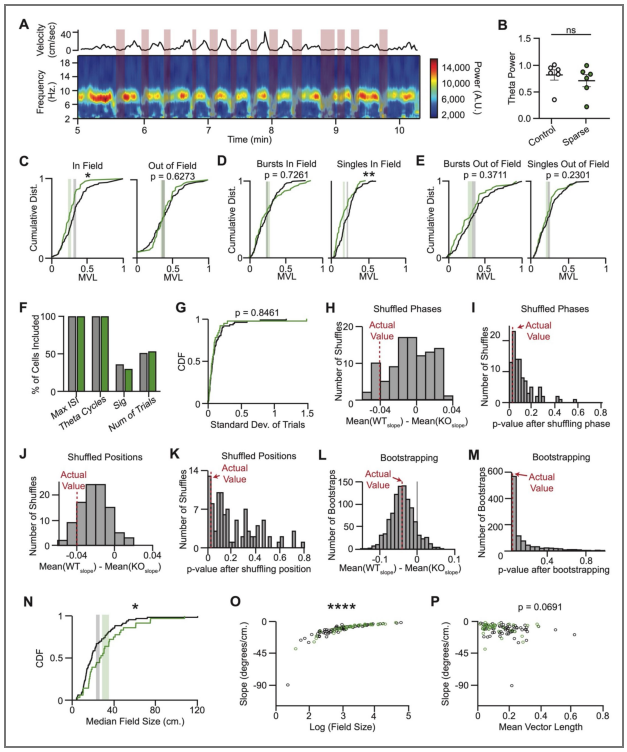

Supplemental Figure 6. Impaired theta modulation in NPAS4 KO neurons is carried by single spikes but not bursts and the accompanying phase precession phenotype is related to differences in the size of the place fields.

(A) Velocity (top) and spectrogram (bottom) for a representative session. Shaded red bars are periods of time when the velocity is below 2 cm/sec. (B) Theta power after accounting for the aperiodic offset (data are mean ± SEM; control N=6 animals, sparse N=8; Kolmogorov–Smirnov test). (C) Cumulative probability distribution of mean vector lengths for the in-field spikes (left) or out-of-field (right) spikes. Gray shaded region: ± SEM for WT, centered at the mean; green shaded region: ± SEM for KO, centered at the mean (WT: N = 138; KO: N = 68; Kolmogorov–Smirnov test). (D) As in (F) but for spikes in a burst that occurred in-field (left) or singles (spikes not in a burst) that occurred in-field (WT: N = 138; KO: N = 68; Kolmogorov–Smirnov test). (E) As in (F) but for spikes in a burst that occurred out-of-field (left) or singles (spikes not in a burst) that occurred out-of-field (WT: N = 138; KO: N = 68; Kolmogorov–Smirnov test). (F) Percentage of neurons retained after sequential thresholding steps applied during phase precession slope estimation. Criteria included: 1. Max ISI - spikes within each trial must have interspike intervals ≤ 1 s; 2. Theta Cycles - trials must span ≥ 3 theta cycles; 3. Sig - trial-level circular-linear regression must yield a p-value < 0.05; 4. Number of Trials - neurons must have ≥ 3 trials meeting the above criteria to be included in downstream analyses (WT: N = 70; KO: N = 36). (G) Cumulative probability distribution of the standard deviation of phase precession slopes across trials for WT and KO neurons. Gray shaded region: ± SEM for WT, centered at the mean; green shaded region: ± SEM for KO, centered at the mean (WT: N = 70; KO: N = 36; Kolmogorov–Smirnov test). (H-K) Shuffle analyses to assess whether the group difference in phase precession slopes reflects structured relationships between spike phase and position. (H) Histogram of mean slope differences (WT minus KO) across 100 iterations of theta phase shuffling, where theta phases were randomly permuted within each trial to disrupt spike–theta alignment. Red dotted line: the value derived from the actual data (WT: N = 70; KO: N = 36). (I) Histogram of p-values from Kolmogorov-Smirnov (KS) tests comparing WT and KO slopes in each phase-shuffled iteration (shuffling as in [H]). Red dotted line: the value derived from the actual data (WT: N = 70; KO: N = 36). (J) As in (H), but for position shuffling, in which spike positions were randomly permuted within trials (WT: N = 70; KO: N = 36). (K) As in (H), but for position shuffling as in [J] (WT: N = 70; KO: N = 36). (L-M) Bootstrapping analysis to estimate the reliability of the observed group difference. (L) Histogram of mean slope differences (WT minus KO) across 1,000 bootstrap iterations, resampling neurons with replacement while maintaining the original sample size per genotype (WT: N = 70; KO: N = 36). (M) Histogram of p-values from Kolmogorov-Smirnov (KS) tests comparing WT and KO slopes in each bootstrap iteration (WT: N = 70; KO: N = 36). (N) Cumulative probability distribution of the median field size for neurons included in the phase precession analysis. Gray shaded region: ± SEM for WT, centered at the mean; green shaded region: ± SEM for KO, centered at the mean (WT: N = 70; KO: N = 36; Kolmogorov–Smirnov test). (O) Relationship between phase precession slope and log-transformed field size across neurons (WT: gray; KO: green; WT: N = 70; KO: N = 36). (P) Relationship between phase precession slope and theta modulation strength (MVL; WT: gray; KO: green; WT: N = 70; KO: N = 36). *p < 0.05; **p < 0.01, ****p < 0.0001.

Model	Predictors	Adjusted R^2	Coefficients	p-Values
1	Genotype only	-0.0050	β (intercept) = 1.8775 β (genotype) = 0.0716	p(intercept) = 3.6432e-43 p(genotype) = 0.6851
2	Theta MVL only	0.0323	β (intercept) = 2.2373 β (theta MVL) = -1.7200	p(intercept) = 1.8350e-31 p(theta MVL) = 0.0110
3	Field size only	0.2710	β (intercept) = -0.8943 β (field size) = 0.9223	p(intercept) = 0.0134 p(field size) = 2.4337e-13
4	Genotype + Field Size + Theta MVL	0.2784	β (intercept) = -0.6398 β (genotype) = -0.2154 β (field size) = 0.9191 β (theta MVL) = -0.8995	p(intercept) = 0.1149 p(genotype) = 0.1643 p(field size) = 1.3433e-12 p(theta MVL) = 0.1333
5	Genotype * Field Size + Genotype * Theta MVL	0.2785	β (intercept) = -0.1919 β (genotype, WT) = -1.3817 β (field size) = 0.7841 β (theta MVL) = -1.1387 β (genotype, KO:field size) = 0.3894 β (genotype, KO:theta MVL) = 0.2785	p(intercept) = 0.7117 p(genotype) = 0.1036 p(field size) = 8.1668e-07 p(theta MVL) = 0.1081 p(genotype:field size) = 0.1613 p(genotype:theta MVL) = 0.7764

Table S1. Linear regression models examining predictors of phase precession slope.

Models were fit using MATLAB's fitlm function. Each model included different combinations of predictors: genotype (WT vs. KO), field size (log-transformed), and theta modulation (log-transform of the mean vector length). The purpose of these models was to determine which variables best account for variability in phase precession slope and to assess the unique contribution of each predictor. Adjusted R^2 values were used to compare model fit while penalizing for model

Acknowledgements

We thank members of the Bloodgood lab for ongoing discussion and input that shaped the direction of this study. We specifically acknowledge Kayla Torres, Destiny Tellez, Jedd Santamaria, Hunter Robbins, Jacob Gerzenshtein, Jerry Hou, Elena Dreisbach, and Paola Guerrero-Servin for assistance with training mice and animal care. We are grateful to all the members of the Leutgebs' lab for thoughtful discussion throughout the development and execution of this study. We specifically thank Sunandha Srikanth, Ipshita Zutshi, Geoff Diehl, Sia Ahmadi, and Li Yuan for their thoughtful discussions and assistance with code used for analyses. The authors acknowledge with gratitude Nicholas Topper, Sarah Burke, and Andrew Maurer for developing the synchronization technique used in this study to align electrophysiology and video recordings. This work was supported by the National Institutes of Health through grants to B.L.B. (NINDS R01 NS111162) and training support to A.P. (NIMH F31 MH123112, NIBIB T32 EB009380, and NINDS T32 NS061847).

Additional information

Author Contributions

Conceptualization, A.P, A.L.H, and B.L.B.; methodology, A.P., C.S., and C.Q.; formal analysis, A.P., C.S., and D.A.H.; investigation, A.P., D.A.H., L.L.H., and R.S.G.; resources, J.K.L., S.L., and B.L.B.; writing - original draft, A.P. and B.L.B.; writing - review and editing, A.P., D.A.H., A.L.H., J.K.L., S.L., and B.L.B.; visualization - A.P.; supervision, J.K.L., S.L., and B.L.B.; funding acquisition – A.P., and B.L.B.

Funding

Funder	Grant reference number	Author
HHS | NIH | National Institute of Neurological Disorders and Stroke (NINDS)	R01 NS111162	Brenda L Bloodgood
HHS | NIH | National Institute of Neurological Disorders and Stroke (NINDS)	T32 NS061847	Anja Payne
HHS | NIH | National Institute of Mental Health (NIMH)	F31 MH123112	Anja Payne
HHS | NIH | National Institute of Biomedical Imaging and Bioengineering (NIBIB)	T32 EB009380	Anja Payne

Author ORCID iDs

Anja Payne: https://orcid.org/0009-0002-0376-5116
Daniel A Heinz: https://orcid.org/0000-0002-9450-6242
Jill K Leutgeb: https://orcid.org/0000-0002-2014-842X
Stefan Leutgeb: https://orcid.org/0000-0003-3367-6536
Brenda L Bloodgood: https://orcid.org/0000-0002-4797-9119

References

1. **Minatohara K,** Akiyoshi M, Okuno H (2015) Role of immediate-early genes in synaptic plasticity and neuronal ensembles underlying the memory trace. *Front. Mol. Neurosci* **8** https://doi.org/10.3389/fnmol.2015.00078 | PubMed
2. **Okuno H** (2011) Regulation and function of immediate-early genes in the brain: beyond neuronal activity markers. *Neurosci. Res* **69**:175-186 https://doi.org/10.1016/j.neures.2010.12.007 | PubMed
3. **Sugo N,** Atsumi Y, Yamamoto N (2025) Transcription and epigenetic factor dynamics in neuronal activity-dependent gene regulation. *Trends Genet* **41**:425-436 https://doi.org/10.1016/j.tig.2024.12.008 | PubMed

4. **Yap E.-L,** Greenberg ME (2018) Activity-regulated transcription: Bridging the gap between neural activity and behavior. *Neuron* **100**:330-348 https://doi.org/10.1016/j.neuron.2018.10.013 | PubMed
5. **Lin Y,** et al. (2008) Activity-dependent regulation of inhibitory synapse development by Npas4. *Nature* **455**:1198-1204 https://doi.org/10.1038/nature07319 | PubMed
6. **Bloodgood BL,** Sharma N, Browne HA, Trepman AZ, Greenberg ME (2013) The activity-dependent transcription factor NPAS4 regulates domain-specific inhibition. *Nature* **503**:121-125 https://doi.org/10.1038/nature12743 | PubMed
7. **Guzowski JF,** McNaughton BL, Barnes CA, Worley PF (1999) Environment-specific expression of the immediate-early gene Arc in hippocampal neuronal ensembles. *Nat. Neurosci* **2**:1120-1124 https://doi.org/10.1038/16046 | PubMed
8. **Guzowski JF,** Setlow B, Wagner EK, McGaugh JL (2001) Experience-Dependent Gene Expression in the Rat Hippocampus after Spatial Learning: A Comparison of the Immediate-Early GenesArc, c-fos, and zif268. *J. Neurosci* **21**:5089-5098 https://doi.org/10.1523/jneurosci.21-14-05089.2001 | PubMed
9. **Vann SD,** Brown MW, Erichsen JT, Aggleton JP (2000) Fos imaging reveals differential patterns of hippocampal and parahippocampal subfield activation in rats in response to different spatial memory tests. *J. Neurosci* **20**:2711-2718 https://doi.org/10.1523/jneurosci.20-07-02711.2000 | PubMed
10. **Hall J,** Thomas KL, Everitt BJ (2001) Cellular imaging of zif268 expression in the hippocampus and amygdala during contextual and cued fear memory retrieval: selective activation of hippocampal CA1 neurons during the recall of contextual memories. *J. Neurosci* **21**:2186-2193 https://doi.org/10.1523/jneurosci.21-06-02186.2001 | PubMed
11. **Ramírez-Amaya V,** et al. (2005) Spatial exploration-induced Arc mRNA and protein expression: evidence for selective, network-specific reactivation. *J. Neurosci* **25**:1761-1768 https://doi.org/10.1523/jneurosci.4342-04.2005 | PubMed
12. **Mamiya N,** et al. (2009) Brain region-specific gene expression activation required for reconsolidation and extinction of contextual fear memory. *J. Neurosci* **29**:402-413 https://doi.org/10.1523/jneurosci.4639-08.2009 | PubMed
13. **Ramamoorthi K,** et al. (2011) Npas4 regulates a transcriptional program in CA3 required for contextual memory formation. *Science* **334**:1669-1675 https://doi.org/10.1126/science.1208049 | PubMed
14. **Shepherd JD,** et al. (2006) Arc/Arg3.1 mediates homeostatic synaptic scaling of AMPA receptors. *Neuron* **52**:475-484 https://doi.org/10.1016/j.neuron.2006.08.034 | PubMed
15. **Chowdhury S,** et al. (2006) Arc/Arg3.1 interacts with the endocytic machinery to regulate AMPA receptor trafficking. *Neuron* **52**:445-459 https://doi.org/10.1016/j.neuron.2006.08.033 | PubMed
16. **Pettit NL,** Yap E.-L, Greenberg ME, Harvey CD (2022) Fos ensembles encode and shape stable spatial maps in the hippocampus. *Nature* **609**:327-334 https://doi.org/10.1038/s41586-022-05113-1 | PubMed
17. **Tanaka KZ,** et al. (2018) The hippocampal engram maps experience but not place. *Science* **361**:392-397 https://doi.org/10.1126/science.aat5397 | PubMed
18. **Ploski JE,** Monsey MS, Nguyen T, DiLeone RJ, Schafe GE (2011) The neuronal PAS domain protein 4 (Npas4) is required for new and reactivated fear memories. *PLoS One* **6**:e23760 https://doi.org/10.1371/journal.pone.0023760 | PubMed
19. **Guo M.-L,** et al. (2012) Upregulation of Npas4 protein expression by chronic administration of amphetamine in rat nucleus accumbens in vivo. *Neurosci. Lett* **528**:210-214 https://doi.org/10.1016/j.neulet.2012.07.048 | PubMed
20. **Heroux NA,** et al. (2018) Differential expression of the immediate early genes c-Fos, Arc, Egr-1, and Npas4 during long-term memory formation in the context preexposure facilitation effect (CPFE). *Neurobiol. Learn. Mem* **147**:128-138 https://doi.org/10.1016/j.nlm.2017.11.016 | PubMed

21. **Martin TA,** et al. (2012) Methamphetamine causes differential alterations in gene expression and patterns of histone acetylation/hypoacetylation in the rat nucleus accumbens. *PLoS One* **7**:e34236 https://doi.org/10.1371/journal.pone.0034236 | PubMed

22. **Hartzell AL,** et al. (2018) NPAS4 recruits CCK basket cell synapses and enhances cannabinoid-sensitive inhibition in the mouse hippocampus. *eLife* **7** https://doi.org/10.7554/elife.35927 | PubMed

23. **Sun X,** et al. (2020) Functionally distinct neuronal ensembles within the memory engram. *Cell* **181**:410-423.e17 https://doi.org/10.1016/j.cell.2020.02.055 | PubMed

24. **Weng F.-J,** et al. (2018) Npas4 is a critical regulator of learning-induced plasticity at mossy fiber-CA3 synapses during contextual memory formation. *Neuron* **97**:1137-1152.e5 https://doi.org/10.1016/j.neuron.2018.01.026 | PubMed

25. **Brito DVC,** et al. (2024) Biphasic Npas4 expression promotes inhibitory plasticity and suppression of fear memory consolidation in mice. *Mol. Psychiatry* **29**:1929-1940 https://doi.org/10.1038/s41380-024-02454-3 | PubMed

26. **Heinz DA,** Cui W, Cooper KL, Bloodgood BL (2025) Experience-induced NPAS4 reduces dendritic inhibition from CCK+ inhibitory neurons and enhances plasticity. *J. Neurophysiol* **134**:361-371 https://doi.org/10.1152/jn.00216.2025 | PubMed

27. **O'Keefe J** (1976) Place units in the hippocampus of the freely moving rat. *Exp. Neurol* **51**:78-109 https://doi.org/10.1016/0014-4886(76)90055-8 | PubMed

28. **O'Keefe J,** Dostrovsky J (1971) The hippocampus as a spatial map. Preliminary evidence from unit activity in the freely-moving rat. *Brain Res* **34**:171-175 https://doi.org/10.1016/0006-8993(71)90358-1 | PubMed

29. **Muller RU,** Kubie JL (1987) The effects of changes in the environment on the spatial firing of hippocampal complex-spike cells. *J. Neurosci* **7**:1951-1968 https://doi.org/10.1523/jneurosci.07-07-01951.1987 | PubMed

30. **Wilson MA,** McNaughton BL (1993) Dynamics of the hippocampal ensemble code for space. *Science* **261**:1055-1058 https://doi.org/10.1126/science.8351520 | PubMed

31. **O'Keefe J,** Recce ML (1993) Phase relationship between hippocampal place units and the EEG theta rhythm. *Hippocampus* **3**:317-330 https://doi.org/10.1002/hipo.450030307 | PubMed

32. **Buzsáki G** (2002) Theta oscillations in the hippocampus. *Neuron* **33**:325-340 https://doi.org/10.1016/s0896-6273(02)00586-x | PubMed

33. **Buzsáki G,** Draguhn A (2004) Neuronal oscillations in cortical networks. *Science* **304**:1926-1929 https://doi.org/10.1126/science.1099745 | PubMed

34. **Skaggs WE,** McNaughton BL, Wilson MA, Barnes CA (1996) Theta phase precession in hippocampal neuronal populations and the compression of temporal sequences. *Hippocampus* **6**:149-172 https://doi.org/10.1002/(sici)1098-1063(1996)6:2<149::aid-hipo6>3.0.co;2-k | PubMed

35. **Buzsáki G,** Moser EI (2013) Memory, navigation and theta rhythm in the hippocampal-entorhinal system. *Nat. Neurosci* **16**:130-138 https://doi.org/10.1038/nn.3304 | PubMed

36. **Maurer AP,** Cowen SL, Burke SN, Barnes CA, McNaughton BL (2006) Organization of hippocampal cell assemblies based on theta phase precession. *Hippocampus* **16**:785-794 https://doi.org/10.1002/hipo.20202 | PubMed

37. **Schmidt R,** et al. (2009) Single-trial phase precession in the hippocampus. *J. Neurosci* **29**:13232-13241 https://doi.org/10.1523/jneurosci.2270-09.2009 | PubMed

38. **Del Pino I,** et al. (2017) Abnormal wiring of CCK+ basket cells disrupts spatial information coding. *Nat. Neurosci* **20**:784-792 https://doi.org/10.1038/nn.4544 | PubMed

39. **Dudok B,** et al. (2024) Retrograde endocannabinoid signaling at inhibitory synapses in vivo. *Science* **383**:967-970 https://doi.org/10.1126/science.adk3863 | PubMed

40. **Rangel Guerrero DK,** et al. (2024) Hippocampal cholecystokinin-expressing interneurons regulate temporal coding and contextual learning. *Neuron* https://doi.org/10.1016/j.neuron.2024.03.019 | PubMed

41. **Lima SQ,** Hromádka T, Znamenskiy P, Zador AM (2009) PINP: a new method of tagging neuronal populations for identification during in vivo electrophysiological recording. *PLoS One* **4**:e6099 https://doi.org/10.1371/journal.pone.0006099 | PubMed

42. **McNaughton BL,** Barnes CA, O'Keefe J (1983) The contributions of position, direction, and velocity to single unit activity in the hippocampus of freely-moving rats. *Exp. Brain Res* **52**:41-49 https://doi.org/10.1007/bf00237147 | PubMed

43. **Markus EJ,** et al. (1995) Interactions between location and task affect the spatial and directional firing of hippocampal neurons. *J. Neurosci* **15**:7079-7094 https://doi.org/10.1523/jneurosci.15-11-07079.1995 | PubMed

44. **Mehta MR,** Quirk MC, Wilson MA (2000) Experience-dependent asymmetric shape of hippocampal receptive fields. *Neuron* **25**:707-715 https://doi.org/10.1016/s0896-6273(00)81072-7 | PubMed

45. **Mehta MR,** Barnes CA, McNaughton BL (1997) Experience-dependent, asymmetric expansion of hippocampal place fields. *Proc. Natl. Acad. Sci. U. S. A* **94**:8918-8921 https://doi.org/10.1073/pnas.94.16.8918 | PubMed

46. **Bittner KC,** Milstein AD, Grienberger C, Romani S, Magee JC (2017) Behavioral time scale synaptic plasticity underlies CA1 place fields. *Science* **357**:1033-1036 https://doi.org/10.1126/science.aan3846 | PubMed

47. **Pelkey KA,** et al. (2017) Hippocampal GABAergic Inhibitory Interneurons. *Physiol. Rev* **97**:1619-1747 https://doi.org/10.1152/physrev.00007.2017 | PubMed

48. **Cobb SR,** Buhl EH, Halasy K, Paulsen O, Somogyi P (1995) Synchronization of neuronal activity in hippocampus by individual GABAergic interneurons. *Nature* **378**:75-78 https://doi.org/10.1038/378075a0 | PubMed

49. **Klausberger T,** et al. (2003) Brain-state- and cell-type-specific firing of hippocampal interneurons in vivo. *Nature* **421**:844-848 https://doi.org/10.1038/nature01374 | PubMed

50. **Klausberger T,** et al. (2005) Complementary roles of cholecystokinin- and parvalbumin-expressing GABAergic neurons in hippocampal network oscillations. *J. Neurosci* **25**:9782-9793 https://doi.org/10.1523/jneurosci.3269-05.2005 | PubMed

51. **O'Neill J,** Senior TJ, Allen K, Huxter JR, Csicsvari J (2008) Reactivation of experience-dependent cell assembly patterns in the hippocampus. *Nat. Neurosci* **11**:209-215 https://doi.org/10.1038/nn2037 | PubMed

52. **Souza BC,** Tort ABL (2017) Asymmetry of the temporal code for space by hippocampal place cells. *Sci. Rep* **7**:8507 https://doi.org/10.1038/s41598-017-08609-3 | PubMed

53. **Mehta MR,** Lee AK, Wilson MA (2002) Role of experience and oscillations in transforming a rate code into a temporal code. *Nature* **417**:741-746 https://doi.org/10.1038/nature00807 | PubMed

54. **Dragoi G,** Buzsáki G (2006) Temporal encoding of place sequences by hippocampal cell assemblies. *Neuron* **50**:145-157 https://doi.org/10.1016/j.neuron.2006.02.023 | PubMed

55. **da Silva Viana,** et al. (2024) Localized APP expression results in progressive network dysfunction by disorganizing spike timing. *Neuron* **112**:124-140.e6 https://doi.org/10.1016/j.neuron.2023.10.001 | PubMed

56. **Huxter J,** Burgess N, O'Keefe J (2003) Independent rate and temporal coding in hippocampal pyramidal cells. *Nature* **425**:828-832 https://doi.org/10.1038/nature02058 | PubMed

57. **Huang L,** et al. (2021) Relationship between simultaneously recorded spiking activity and fluorescence signal in GCaMP6 transgenic mice. *eLife* **10** https://doi.org/10.7554/elife.51675 | PubMed

58. **Zhang Y,** et al. (2023) Fast and sensitive GCaMP calcium indicators for imaging neural populations. *Nature* **615**:884-891 https://doi.org/10.1038/s41586-023-05828-9 | PubMed

59. **Lovett-Barron M,** et al. (2012) Regulation of neuronal input transformations by tunable dendritic inhibition. *Nat. Neurosci* **15**:423-30 https://doi.org/10.1038/nn.3024 | PubMed

60. **Müllner FE,** Wierenga CJ, Bonhoeffer T (2015) Precision of inhibition: Dendritic inhibition by individual GABAergic synapses on hippocampal pyramidal cells is confined in space and time. *Neuron* **87**:576-589 https://doi.org/10.1016/j.neuron.2015.07.003 | PubMed

61. **Bittner KC,** et al. (2015) Conjunctive input processing drives feature selectivity in hippocampal CA1 neurons. *Nat. Neurosci* **18**:1133-1142 https://doi.org/10.1038/nn.4062 | PubMed

62. **Grienberger C,** Milstein AD, Bittner KC, Romani S, Magee JC (2017) Inhibitory suppression of heterogeneously tuned excitation enhances spatial coding in CA1 place cells. *Nat. Neurosci* **20**:417-426 https://doi.org/10.1038/nn.4486 | PubMed

63. **Basu J,** et al. (2016) Gating of hippocampal activity, plasticity, and memory by entorhinal cortex long-range inhibition. *Science* **351** https://doi.org/10.1126/science.aaa5694 | PubMed

64. **Basu J,** et al. (2013) A cortico-hippocampal learning rule shapes inhibitory microcircuit activity to enhance hippocampal information flow. *Neuron* **79**:1208-1221 https://doi.org/10.1016/j.neuron.2013.07.001 | PubMed

65. **Gasparini S,** Magee JC (2006) State-dependent dendritic computation in hippocampal CA1 pyramidal neurons. *J. Neurosci* **26**:2088-2100 https://doi.org/10.1523/jneurosci.4428-05.2006 | PubMed

66. **Jarsky T,** Roxin A, Kath WL, Spruston N (2005) Conditional dendritic spike propagation following distal synaptic activation of hippocampal CA1 pyramidal neurons. *Nat. Neurosci* **8**:1667-1676 https://doi.org/10.1038/nn1599 | PubMed

67. **Takahashi H,** Magee JC (2009) Pathway interactions and synaptic plasticity in the dendritic tuft regions of CA1 pyramidal neurons. *Neuron* **62**:102-111 https://doi.org/10.1016/j.neuron.2009.03.007 | PubMed

68. **Tsay D,** Dudman JT, Siegelbaum SA (2007) HCN1 channels constrain synaptically evoked Ca2+ spikes in distal dendrites of CA1 pyramidal neurons. *Neuron* **56**:1076-1089 https://doi.org/10.1016/j.neuron.2007.11.015 | PubMed

69. **Priestley JB,** Bowler JC, Rolotti SV, Fusi S, Losonczy A (2022) Signatures of rapid plasticity in hippocampal CA1 representations during novel experiences. *Neuron* **110**:1978-1992.e6 https://doi.org/10.1016/j.neuron.2022.03.026 | PubMed

70. **Klausberger T,** Somogyi P (2008) Neuronal diversity and temporal dynamics: the unity of hippocampal circuit operations. *Science* **321**:53-57 https://doi.org/10.1126/science.1149381 | PubMed

71. **Robbe D,** Buzsáki G (2009) Alteration of theta timescale dynamics of hippocampal place cells by a cannabinoid is associated with memory impairment. *J. Neurosci* **29**:12597-12605 https://doi.org/10.1523/jneurosci.2407-09.2009 | PubMed

72. **Losonczy A,** Zemelman BV, Vaziri A, Magee JC (2010) Network mechanisms of theta related neuronal activity in hippocampal CA1 pyramidal neurons. *Nat. Neurosci* **13**:967-972 https://doi.org/10.1038/nn.2597 | PubMed

73. **Dudok B,** et al. (2021) Alternating sources of perisomatic inhibition during behavior. *Neuron* **109**:997-1012.e9 https://doi.org/10.1016/j.neuron.2021.01.003 | PubMed

74. **Geiller T,** et al. (2020) Large-Scale 3D Two-Photon Imaging of Molecularly Identified CA1 Interneuron Dynamics in Behaving Mice. *Neuron* **108**:968-983.e9 https://doi.org/10.1016/j.neuron.2020.09.013 | PubMed

75. **Yap E.-L,** et al. (2021) Bidirectional perisomatic inhibitory plasticity of a Fos neuronal network. *Nature* **590**:115-121 https://doi.org/10.1038/s41586-020-3031-0 | PubMed

76. **Ting JT,** et al. (2018) Preparation of Acute Brain Slices Using an Optimized N-Methyl-D-glucamine Protective Recovery Method. *J. Vis. Exp* https://doi.org/10.3791/53825 | PubMed

77. **Pologruto TA,** Sabatini BL, Svoboda K (2003) ScanImage: flexible software for operating laser scanning microscopes. *Biomed Eng Online* **2** https://doi.org/10.1186/1475-925x-2-13 | PubMed

78. **Rothman JS,** Silver RA (2018) NeuroMatic: An Integrated Open-Source Software Toolkit for Acquisition, Analysis and Simulation of Electrophysiological Data. *Front. Neuroinform* **12** https://doi.org/10.3389/fninf.2018.00014 | PubMed

79. **Anikeeva P,** et al. (2011) Optetrode: a multichannel readout for optogenetic control in freely moving mice. *Nat. Neurosci* **15**:163-170 https://doi.org/10.1038/nn.2992 | PubMed

80. **Topper NC,** Burke SN, Maurer AP (2014) Multiple frequency audio signal communication as a mechanism for neurophysiology and video data synchronization. *J. Neurosci. Methods* **238**:35-42 https://doi.org/10.1016/j.jneumeth.2014.09.018 | PubMed

Peer reviews

Reviewer #1 (Public review):

Summary:

NPAS4 is an activity-dependent transcription factor that regulates inhibitory synapses onto active pyramidal neurons. In this study, the authors examined whether this molecular mechanism influences neural coding in awake animals. To accomplish this, they generated a sparse, CA1-specific NPAS4 knockout in mice and compared knockout neurons with neighboring wild-type neurons recorded from the same animals during navigation. They found that, although neurons lacking NPAS4, which received diminished somatic inhibition and enhanced dendritic inhibition, still encoded location, their spatial firing was less precise: place fields were broader and less stable, showed weaker firing within the field, and exhibited more firing outside the field. KO neurons also exhibited poorer temporal organization with weaker coupling to theta oscillations and reduced phase precession, two signatures of precise spike timing in the hippocampus. Overall, the study suggests that NPAS4 links the balance of somatic and dendritic inhibition to the quality of circuit-level coding by refining the spatial and temporal precision of neuronal firing.

Strengths:

Using a sparse CA1-specific knockout, the authors compared NPAS4-deficient neurons with neighboring wild-type neurons within the same animal and network. This is a significant advantage because it minimizes confounding factors arising from global circuit disruption, providing a clearer comparison of genotypes. Furthermore, the rigorous optogenetic tagging strategy used to distinguish KO from WT neurons in vivo makes the single-cell comparisons much more convincing. Electrophysiological recordings from intermingled WT and KO neurons enable precise spike-timing measurements relative to a shared local field potential, which would be challenging to obtain with calcium imaging.

Weaknesses:

Rather than an acute manipulation, the authors rely on a chronic, sparse knockout, and NPAS4 had been deleted for at least one month before recording. Consequently, while the paper demonstrates a robust long-term phenotype, it is less definitive about the immediate causal sequence by which NPAS4 induction alters inhibition and reshapes spatial and temporal coding. Furthermore, the study focuses on single-neuron coding during navigation and does not test whether the observed degradation in coding precision leads to corresponding impairments in learning or memory in the same animals. In the discussion, the authors suggest that NPAS4 may be especially important for ripple-associated activity during sleep; however, the paper does not test this possibility.

https://doi.org/10.7554/eLife.111430.1.sa2

Reviewer #2 (Public review):

Summary:

The manuscript by Payne and colleagues examines how cell-autonomous loss of the activity-dependent transcription factor NPAS4 reshapes spatial and temporal coding in CA1 pyramidal neurons of behaving mice. The work builds on the Bloodgood lab's established framework in which NPAS4 reorganizes inhibition along the somatodendritic axis of CA1 pyramidal cells, principally by regulating CCK+ basket cell synapses, and asks whether this transcriptionally driven reconfiguration of inhibition propagates into the spike-train statistics that underlie hippocampal function. The combination of sparse Cre delivery with channelrhodopsin-mediated optotagging in Npas4 fl/fl:Ai32 mice is technically elegant, as it permits within-animal comparisons of intermingled wild-type and knockout pyramidal neurons sharing a common LFP, which is a significant analytical advantage for spike-timing analyses and for controlling network-level confounds. The reported phenotype is internally consistent and converges on a coherent story: knockout neurons exhibit broader and less stable place fields, lower signal-to-noise within fields, increased out-of-field activity, weaker theta-phase coupling, and shallower phase precession slopes, with the temporal deficits at least partly explained by enlargement of the spatial receptive field.

Strengths:

Several aspects of the work deserve explicit recognition. The validation of the optotagging strategy is thorough, including the high-power stimulation control to corroborate WT classification and the post hoc histological alignment of GFP+ density with electrophysiologically identified KO fractions. The decision to test NPAS4 function in adult mice maintained in long-term enriched environments addresses an important gap, since most prior work has focused on juveniles or short-term induction paradigms. The acute slice recordings recapitulating the somatodendritic inhibition phenotype reassure the reader that the in vivo measurements are interpreted against a known synaptic substrate. The analytical framework, especially the difference maps across epochs and the linear regression decomposition of phase precession slope into genotype, field size, and theta modulation strength, is rigorous and goes beyond simple group-level comparisons. The conceptual contribution, namely the demonstration that an activity-dependent transcription factor can be tied to single-neuron coding properties in vivo, is meaningful, although it is fair to note that the direction of the effect, given that the CCK to place cell link and the NPAS4 to CCK link have each been established in prior independent studies, is largely along the lines one would predict.

Weaknesses:

The most consequential concern, in my view, is the experimental context in which the entire study is conducted. Every animal is housed in an enriched environment for two to three months, and Figure 1A itself shows that NPAS4 expression in CA1 is essentially undetectable in standard-environment conditions and only emerges with enrichment. This raises the question of whether the manuscript is in fact describing the function of NPAS4 in general, or the function of NPAS4 specifically as recruited by chronic enrichment. The paper, in its current framing, elides this distinction and presents the EE state as if it were the baseline, which it is not. EE is known to alter hippocampal connectivity, the dynamics of place cell ensembles, and the expression of many activity-dependent genes; the CCK to pyramidal cell connectivity that the authors invoke as the mechanistic anchor is also dense in standard housing, so the absence of detectable NPAS4 in SE conditions raises the further conceptual problem of how NPAS4-negative neurons would normally be innervated by CCK+ basket cells in the first place. A direct comparison of WT and KO neurons in standard-environment animals, even on a smaller scale, would discriminate between two very different

interpretations, namely that NPAS4 has a constitutive role in tuning CA1 firing versus that it is specifically engaged by enrichment-driven activity and contributes to an EE-specific reorganization of coding. Recent work, including Chiaruttini and colleagues (2025), reports baseline NPAS4 expression in CA1, so the SE result in Figure 1A may itself underestimate normal expression and deserves further scrutiny. Without an SE comparison, the generality of the conclusions cannot be assessed, and the title and abstract risk overstating the scope of the findings, particularly when one considers that NPAS4 is also induced by contextual fear conditioning and other paradigms, which would predict context-specific effects rather than a uniform refinement function.

A closely related concern is the meaning of the knockout itself. Even under EE, only a few percent of CA1 pyramidal neurons express detectable NPAS4 at any given moment (Figure 1A), yet the AAV strategy deletes the gene in 30 to 60 percent of pyramidal neurons. In effect, the majority of cells classified as KO in this study would not have been expressing the protein under the relevant conditions, so the population that is statistically driving the WT versus KO differences must include a non-trivial fraction of neurons in which the deletion has no protein-level consequence. This dilutes the expected effect and raises a more interesting biological question: are the observed phenotypes carried by the few KO neurons that would have expressed NPAS4, or do they emerge from a constitutive function of the gene that is broader than the IHC signal suggests? An additional, related possibility is that NPAS4 expression segregates non-uniformly across functional classes, for example, concentrating in cells with particular firing-rate or spatial-tuning profiles, in which case the "KO" label is binary at the level of the manipulation but graded at the level of biological consequence. Stratifying the KO population by some proxy of activity history, or relating the magnitude of the phenotype to per-cell measures of recent firing, would help address this. As written, the manuscript treats the KO designation as homogeneous, while the underlying biology is almost certainly not.

A third concern, more conventionally statistical, is the treatment of cells as independent observations. The analyses rely almost uniformly on Kolmogorov-Smirnov tests applied to individual units pooled across animals, but cells recorded in the same animal share not only a common subject but a common network, since WT and KO neurons here are intermingled in the same CA1 microcircuit. Cell numbers per animal range widely, so a mixed-effects framework treating animal as a random factor, or a hierarchical bootstrap, would clarify which effects are robust against animal-level and session-level variability and protect against pseudo-replication. This concern is particularly acute for the smaller effects in Figure 2C-E, where the cumulative distributions overlap substantially, and the differences could plausibly be driven by a small number of mice or sessions. In several figures, the individual dots in supplementary panels are not labeled by animal or session, and that information would be useful for assessing how much of each effect is carried by which subset of the cohort.

The absence of a Cre/ChR2 expression control is a separate gap. The comparison throughout the manuscript pits Cre+ ChR2+ neurons (NPAS4 KO) against neighboring non-transduced neurons (WT). This is internally elegant, but leaves open the possibility that part of the phenotype arises from chronic ChR2 expression or constitutive Cre activity rather than from NPAS4 loss, especially given that most of the readouts are subtle. A small companion cohort of Ai32 mice without the floxed Npas4 allele, injected with the same AAV and processed through identical optotagging and electrophysiology pipelines, would address this definitively and is, in my view, a near-essential addition.

Several of the downstream phenotypes would benefit from stratified comparisons that hold first-order properties constant. Many of the downstream differences (stability across epochs, theta coupling, phase precession) could, in principle, be inherited from the upstream difference in firing rate, since the high-firing and high-spatial-information cells in the WT pool are likely contributing disproportionately to the group statistics. The authors do perform

firing-rate-matched controls in Figure S4D-G, which is helpful, but the analysis should be extended in two ways: a parallel stratification by spatial information for the stability analyses in Figure 4, and matched comparisons of theta coupling (Figure 5) and phase precession (Figure 6) on neurons drawn from overlapping firing-rate and spatial-information distributions. The regression decomposition for phase precession is a step in this direction and shows that field size, not genotype, is the dominant predictor of slope; this finding, in my reading, deserves more prominent framing in the discussion than it currently receives, since it implies that the temporal precision phenotype is largely downstream of the spatial one rather than a parallel deficit.

The place field stability analysis is interesting but somewhat under-analyzed. The authors show that KO fields shift toward the field entrance more rapidly than WT fields and propose that this reflects an accelerated or dysregulated Mehta-effect-like dynamic. The framing is attractive, but the analysis does not establish that the shifts are systematic in the same way the classical Mehta effect is. An alternative reading is that the elevated out-of-field firing creates spurious local maxima that the peak-finding procedure occasionally classifies as field shifts, especially when in-field firing is reduced. A control analysis using a fixed reference window around the original peak, rather than re-identifying the peak each epoch, would help distinguish a genuine plasticity-like shift from instability driven by noise. The behavior of the WT population in epoch 4 also raises a question: would the drift intensify over longer recording windows, and to what extent is the apparent drift imposed by the repetitive structure of the task itself, in which animals are effectively running on a constrained linear /circular track that may impose drift-like dynamics across the population independently of genotype?

A final note on mechanism. The manuscript leans on prior work showing that NPAS4 regulates CCK+ basket cell synapses, and uses this as the mechanistic anchor for the coding deficits. The connection is reasonable but remains indirect within this study, since the authors do not measure CCK+ interneuron activity, perisomatic inhibition, or local circuit dynamics in the same animals. The discussion already acknowledges some of this, but the speculative framing of dendritic versus somatic inhibition contributions could be tightened, especially given that competing inhibitory sources (PV+ basket cells, axo-axonic cells, OLM interneurons) also shape the spatial and temporal features measured here. A more cautious mechanistic framing, distinguishing what is demonstrated from what is inferred from prior work, would be appropriate.

In summary, this is an ambitious and technically demanding study that makes a meaningful contribution by linking activity-dependent transcriptional regulation of inhibition to the spatial and temporal organization of CA1 spike trains in awake, behaving mice. The within-animal optotagging design is a real strength, the phenotype is internally consistent across multiple coding metrics, and the conceptual implications for how experience tunes single-neuron coding are significant. The principal concerns, namely the unaddressed enrichment confound that pervades the entire dataset, the conceptual ambiguity around what a KO designation actually means at the cell level when only a small fraction of CA1 neurons express the protein, the statistical treatment of nested observations from a shared microcircuit, the missing transgene control, the absence of stratified comparisons by firing rate and spatial information for the secondary phenotypes, and the somewhat overreaching mechanistic framing of the discussion, are all addressable, and if handled carefully would substantially strengthen the manuscript. With these revisions, the work would be a valuable contribution to the literature on how the molecular memory of activity shapes circuit-level coding.

https://doi.org/10.7554/eLife.111430.1.sa1

Author response:

We appreciate the time and attention to our manuscript and the feedback from the reviewers, who were overall supportive of the work. Both reviewers validated the technical approach we used to differentiate the wild-type (WT) and knockout (KO) neurons noting: “The combination of sparse Cre delivery with channel rhodopsin-mediated optotagging in Npas4 fl/fl:Ai32 mice is technically elegant” and “the rigorous optogenetic tagging strategy used to distinguish KO from WT neurons *in vivo* makes the single-cell comparisons much more convincing.” Furthermore, they note the consistency of the reported results, stating: “The reported phenotype is internally consistent and converges on a coherent story”.

Both reviewers also pointed out several concerns or points of improvement for the manuscript. Below, we first offer several scientific and methodological clarifications that we believe resolve a number of the reviewers' concerns. We then outline which remaining points we plan to address through revision, and which fall outside the scope of the current study.

Scientific Clarifications:

Request for a standard housing control. Both of the reviewers brought up the long-term enrichment paradigm (EE) we opted to use for this study and expressed interest in seeing data from standard housed (SE) animals. This is an approach the lab has taken in its slice physiology work [1-3], where comparing EE and SE conditions has revealed important differences between cellular phenotype. However, the *in vivo* experiments described here differ in a key way: obtaining these recordings requires extensive handling, training, and daily transport between the vivarium, home cage, and behavior room. These experimental steps themselves constitute the kind of novel, salient experience known to induce NPAS4, making a true SE comparison unattainable within this paradigm. In our experiment, mice were housed in EE as a supplemental, well-established strategy to induce NPAS4 in CA1 pyramidal neurons but we believe the behavior alone would be sufficient. We will describe this more clearly in the text of the manuscript.

Consistent with this view, place fields recorded from wild-type mice in other studies using SE but undergoing comparable handling and training procedures, are similar in size, spatial information, and stability to the WT place fields we reported here [4,5]. As part of our revisions, we will consider statistical comparisons between our WT neurons and those reported in other studies to quantitatively assess whether a difference exists.

More broadly, we note that the existing literature on NPAS4 induction does not, to our knowledge, establish a baseline level of NPAS4 expression in CA1 pyramidal neurons in the complete absence of behavioral experience. Reports of NPAS4 expression in CA1 have generally relied on animals exposed to some form of salient or novel experience [3,6,7], consistent with our framework that NPAS4 induction reflects behaviorally-driven activity rather than a constitutive baseline.

Expression profile of NPAS4. Reviewer #2 brought up a concern about the extent of the NPAS4 expression, referring to the IHC results in Figure 1A stating: “Even under EE, only a few percent of CA1 pyramidal neurons express detectable NPAS4 at any given moment (Figure 1A), yet the AAV strategy deletes the gene in 30 to 60 percent of pyramidal neurons. In effect, the majority of cells classified as KO in this study would not have been expressing the protein under the relevant conditions.” We wish to clarify two points here. First, in the experimental paradigm used to obtain the IHC results, mice were exposed to enrichment for only 90 minutes while in the *in vivo* physiology paradigm, mice were housed in an enriched environment (with frequent toy changes to ensure novelty) for weeks. Thus, NPAS4 is almost certainly expressed in a much larger percentage of WT neurons in mice that were kept in chronic enrichment and used for the *in vivo* studies. Second, while the NPAS4 protein is only

expressed in cells for several hours following neuronal activity, it initiates an inhibitory synapse phenotype that persists long-term. Thus, even though a small percentage of neurons are NPAS4+ in the IHC results, it is likely that a much larger percentage of them have expressed NPAS4 in the past and now show the inhibitory synapse phenotype. Evidence for this comes from the slice physiology results in Figure 1C (and see similar results from adolescents [1-3]) in which animals were housed in enrichment long-term and differences between inhibition persisted in nearly every WT/KO comparison.

We also recognize the related possibility that NPAS4 expression may not be uniform across the pyramidal cell population, but may instead concentrate in particular functional subtypes, such as cells with higher firing rates or stronger spatial tuning. As part of our revisions, we plan to test this directly by stratifying the KO population by firing rate and relating it to the magnitude of the observed phenotype. Taken together, we believe that while only a small fraction of CA1 pyramidal neurons are NPAS4+ at any given moment, a much larger fraction have experienced NPAS4 induction and the accompanying synaptic reorganization over the timescale of chronic enrichment making the WT/KO comparison in this study substantially less diluted than the IHC snapshot alone would suggest.

Timeline of NPAS4 expression and synaptic reorganization. Reviewer #1 pointed out that this study only examines the effects of NPAS4-deletion on longer timescales (weeks to months after the virus expression and subsequent knockout) stating “[the study] is less definitive about the immediate causal sequence by which NPAS4 induction alters inhibition and reshapes spatial and temporal coding”. The reviewer is correct, the temporal relationship between NPAS4 expression, changes in synaptic inhibition, and changes in neuronal firing are important outstanding questions in the field. Currently, we lack molecular tools that would enable us to clearly test these relationships but with our existing, albeit limited information, we have the following working model.

When an animal is placed into a new context, a subset of CA1 pyramidal neurons will fire action potentials in a spatially refined manner. This activity will drive NPAS4 expression in those neurons, resulting in protein expression that persists for a couple of hours before the protein is degraded.

Following expression, NPAS4 will bind to various sites in the genome and initiate a genetic program which results in changes in inhibition recruiting CCK basket cell synapses to the soma and destabilizing CCK dendritic synapses. The exact mechanism behind this reorganization of inhibition is unknown, but the phenotype likely emerges over the course of several hours following NPAS4 expression and persists for days following the stimulus that induced NPAS4.

While our chronic knockout approach does not allow us to resolve the precise timing of events in this sequence, it does allow us to ask a distinct and complementary question: what is the long-term consequence for a neuron that has never been able to execute this program? Our results demonstrate that NPAS4-deficient neurons which cannot initiate NPAS4-dependent inhibitory reorganization regardless of their activity history show systematic degradation in spatial and temporal coding precision. This establishes that the NPAS4-dependent inhibitory phenotype has lasting and functionally meaningful consequences for *in vivo* information encoding, a question that shorter-timescale or acute manipulations would not be well-positioned to address. Resolving the immediate causal sequence between NPAS4 induction, synaptic reorganization, and changes in firing will be an important goal for future work as new molecular tools become available.

Behaviors that drive NPAS4 expression. Reviewer #2 pointed out that “NPAS4 is also induced by contextual fear conditioning and other paradigms which would predict context-specific effects rather than a uniform refinement function.” They are correct NPAS4 is expressed in response to different behavioral paradigms, including fear conditioning and environmental

enrichment. However, the subregion in which NPAS4 is induced depends critically on the behavioral paradigm. When mice are exposed to contextual fear conditioning, NPAS4 expression is robust in CA3 and the dentate gyrus but negligible in CA1 [6]. This is consistent with the known activity patterns of these subregions: CA3 neurons are strongly recruited during contextually-dependent associative learning, while CA1 neurons are more reliably driven by exposure to novelty and respond in a spatially-refined manner. Consistent with this, studies using fear conditioning have focused on behavioral discrimination and synaptic changes in CA3 and granule cells [6]. To our knowledge no study has examined the relationship between fear conditioning, NPAS4, and CA1 pyramidal neuron function. Whether behavioral paradigms beyond environmental enrichment and spatial navigation can induce NPAS4 in CA1, and what consequences that might have for pyramidal neuron firing, are interesting questions for future work.

We also wish to address the conceptual framing underlying this concern. In CA1, we do not believe that “context-specific effects” are separable from a “uniform refinement function.” CA1 pyramidal neurons respond in a context-dependent manner. When a mouse is placed onto a linear track, there is a subset of neurons that will increase their activity over the course of that exposure. But within this subset, individual neurons will also show spatially-refined responses firing action potentials as the animal runs through the corresponding place field. The spatial precision NPAS4 confers is always nested within context-dependent mechanisms NPAS4 refines whatever representation a neuron is already computing, rather than overriding the context-dependency of that representation. We therefore do not view these as competing frameworks.

The role of NPAS4 in shaping CCK synapses. Reviewer #2 made the point that “the CCK to pyramidal cell connectivity that the authors invoke as the mechanistic anchor is also dense in standard housing, so the absence of detectable NPAS4 in SE conditions raises the further conceptual problem of how NPAS4-negative neurons would normally be innervated by CCK+ basket cells in the first place.” We wish to clarify that NPAS4 is not necessary for the formation of CCK synapses onto CA1 pyramidal neurons there are likely a number of NPAS4-independent mechanisms that regulate this synaptic connectivity (for example, see [8]). Rather, we place NPAS4 in the role of an activity-dependent modulator that acts on top of this baseline connectivity: when NPAS4 is expressed in response to neuronal activity, it shifts the balance of CCK inhibitory input along the somatodendritic axis, increasing somatic and decreasing dendritic CCK synaptic strength [1,2]. The question is therefore not how CCK synapses are established in the absence of NPAS4, but rather how experience-dependent activity uses NPAS4 to fine-tune the distribution of those synapses and it is this fine-tuning that our study links to the precision of *in vivo* spatial and temporal coding.

Methodological Clarifications:

Clarification on how stability analysis was performed. Reviewer #2 requested additional analysis for the stability results: “A control analysis using a fixed reference window around the original peak, rather than re-identifying the peak each epoch, would help distinguish a genuine plasticity-like shift from instability driven by noise.” We wish to clarify that this is precisely the methodology that was used in the manuscript. For the stability analysis shown in Figures 4C-E, the activity was aligned to the peak activity in epoch 1 such that 0 always represents the location of the peak in epoch 1. This approach allows us to identify how that activity differs in subsequent epochs, namely whether it has shifted relative to the activity in epoch 1. We will make this more clear in the results and methods sections.

Request for Ai32 control. Reviewer #2 made the point that “The comparison throughout the manuscript pits Cre+ ChR2+ neurons (NPAS4 KO) against neighboring non-transduced neurons (WT). This is internally elegant, but leaves open the possibility that part of the phenotype arises from chronic ChR2 expression or constitutive Cre activity rather than from NPAS4 loss, especially given that most of the readouts are subtle.” We agree this would be the

ideal control and regret that it is no longer experimentally feasible, as the laboratory in which these experiments were conducted is no longer operating. However, we believe several features of the existing dataset make a ChR2 or Cre artifact unlikely. First, the effects of chronic ChR2 expression are not known to produce the specific pattern of phenotypes we observe in particular the redistribution of somatic versus dendritic inhibition, which is recapitulated independently in acute slice recordings from animals that did not undergo optotagging procedures (Figure 1C). Second, the phenotype we report is internally coherent across multiple independent metrics: place field size, stability, signal-to-noise ratio, theta coupling, and phase precession all shift in the same direction, in a manner consistent with a specific change in inhibitory synaptic balance rather than a nonspecific effect of transgene expression. Third, the sparse nature of the Cre expression means that KO and WT neurons share the same local network, same LFP, and same behavioral context any network-level effect of Cre or ChR2 would be expected to affect both populations similarly. We will add a discussion of these points to the manuscript.

PSTH clarification (unit of opto-response). To quantify the opto-response, we treated each light-on + light-off period (a total of 2 seconds) as the one trial. We aligned the trials by the light-on period, binned the spikes by 1 msec bins, and then summed the responses across trials to produce a histogram. From this histogram we found the maximum response during light off (e.g. the 1 msec bin with the greatest response which should be reported as number of spikes). We subtracted this from the maximum response during light on. Thus, the unit of opto-response should be spike counts. We will clarify this in the text and figures.

Use of male mice. Reviewer #1 rightfully pointed out that this study only used male mice. In this study, we only used mice that were larger than 20 grams to ensure the mice could carry the weight of the implanted drives while performing the behavior. As this genetic line of mice is on the smaller size, only male mice were above this weight threshold. Importantly, slice work conducted in the Blood good lab has not identified sex differences in NPAS4 phenotypes [3,9]. Future studies would benefit from the use of both male and female mice. We will state this more explicitly in the text and expand on the potential implications of excluding female mice from our study.

Future planned changes to manuscript:

As the reviewers suggested, we intend to add the following analyses and make the following changes to the manuscript:

Stratify key analyses (stability, theta coupling, phase precession) by FR to determine whether there is a dependency on the firing rate of cells.

Apply hierarchical bootstrapping and add per-animal color-coding to supplementary figures to assess animal-level variability and protect against pseudoreplication.

Add a circular-linear phase-position correlation analysis as an additional quantification of phase precession strength, complementing the existing slope-based analysis.

Improve discussion around the temporal phenotype being downstream of the spatial one.

Tighten mechanistic framing in the Discussion to more clearly distinguish what is demonstrated in this study from what is inferred from prior work, and to acknowledge the contributions of other inhibitory cell types.

Minor changes and figure clarifications as noted by reviewers.

Outside of the scope of this study or unable to be performed:

There were several recommendations or points that the reviewers brought up that we do not have the resources to address. Nevertheless, we appreciate the reviewers noting these.

SE control (as discussed above)

Ai32 control (as discussed above)

Behavioral consequences of NPAS4 knockout and the effects on learning and memory • Ripple analysis

Drift observed in E4 and what this might look like over larger timescales

Comparison between male and female mice to determine whether there are sex-dependence differences

In conclusion, the reviewers recognized this as a well-designed and internally consistent study. We believe that many of the critiques including the request for a standard housing control, questions regarding the extent of NPAS4 expression across the pyramidal cell population, and points about the timeline of NPAS4 expression and synaptic reorganization are addressed by the clarifications provided in this response. We agree with many of the suggested analytical and textual changes and look forward to incorporating those into the revised manuscript.

References:

(1) Heinz, D. A., Cui, W., Cooper, K. L. & Bloodgood, B. L. Experience-induced NPAS4 reduces dendritic inhibition from CCK+ inhibitory neurons and enhances plasticity. J. Neurophysiol. 134, 361–371 (2025).

(2) Hartzell, A. L. et al. NPAS4 recruits CCK basket cell synapses and enhances cannabinoid-sensitive inhibition in the mouse hippocampus. Elife 7, (2018).

(3) Bloodgood, B. L., Sharma, N., Browne, H. A., Trepman, A. Z. & Greenberg, M. E. The activity dependent transcription factor NPAS4 regulates domain-specific inhibition. Nature 503, 121–125 (2013).

(4) Sharif, F., Tayebi, B., Buzsáki, G., Royer, S. & Fernandez-Ruiz, A. Subcircuits of deep and superficial CA1 place cells support efficient spatial coding across heterogeneous environments. Neuron 109, 363–376.e6 (2021).

(5) Quirk, C. R. et al. Precisely timed theta oscillations are selectively required during the encoding phase of memory. Nat. Neurosci. 24, 1614–1627 (2021).

(6) Ramamoorthi, K. et al. Npas4 regulates a transcriptional program in CA3 required for contextual memory formation. Science 334, 1669–1675 (2011).

(7) Chiaruttini, N. et al. ABBA+BraiAn, an integrated suite for whole-brain mapping, reveals brain-wide differences in immediate-early genes induction upon learning. Cell Rep. 44, 115876 (2025).

(8) Früh, S. et al. Neuronal Dystroglycan Is Necessary for Formation and Maintenance of Functional CCK-Positive Basket Cell Terminals on Pyramidal Cells. J. Neurosci. 36, 10296–10313 (2016).

(9) Lin, Y. et al. Activity-dependent regulation of inhibitory synapse development by Npas4. Nature 455, 1198–1204 (2008).

https://doi.org/10.7554/eLife.111430.1.sa0